Math Geosci (2008) 40: 533–573
DOI 10.1007/s11004-008-9171-7

SPECIAL ISSUE

Anisotropic Scaling Models of Rock Density and the Earth's Surface Gravity Field

S. Lovejoy · H. Gaonac'h · D. Schertzer

Received: 1 August 2007 / Accepted: 8 May 2008 / Published online: 24 June 2008

Abstract In this paper we consider an anisotropic scaling approach to understanding rock density and surface gravity which naturally accounts for wide range variability and anomalies at all scales. This approach is empirically justified by the growing body of evidence that geophysical fields including topography and density are scaling over wide range ranges. Theoretically it is justified, since scale invariance is a (geo)dynamical symmetry principle which is expected to hold in the absence of symmetry breaking mechanisms. Unfortunately, to date most scaling approaches have been self-similar, i.e., they have assumed not only scale invariant but also isotropic dynamics. In contrast, most nonscaling approaches recognize the anisotropy (e.g., the strata), but implicitly assume that the latter is independent of scale. In this paper, we argue that the dynamics are scaling but highly anisotropic, i.e., with scale dependent differential anisotropy.

By using empirical density statistics in the crust and a statistical theory of high Prandtl number convection in the mantle, we argue that $P(\underline{K}, k_z) \approx (|K/k_s|^{H_z} + |k_z/k_s|)^{-s/H_z}$ is a reasonable model for the 3-D spectrum ($\underline{K}$ is the horizontal wavevector and K is its modulus, k_z is a vertical wavenumber), (s, H_z) are fundamental exponents which we estimate as $(5.3, 3)$, $(3, 3)$ in the crust and mantle, respectively. We theoretically derive expressions for the corresponding surface gravity spectrum. For scales smaller than $\approx$100 km, the anisotropic crust model of the density (with flat top and bottom) using empirically determined vertical and horizontal density spectra is sufficient to explain the (Bouguer) g_z spectra. However, the crust

---

S. Lovejoy (✉)
Physics, McGill University, 3600 University st., Montreal, PQ H3A 2T8, Canada
e-mail: lovejoy@physics.mcgill.ca

S. Lovejoy · H. Gaonac'h
GEOTOP, UQAM, C.P. 8888, Succursale Centre Ville, Montreal, PQ H3C 3P8, Canada

D. Schertzer
Université Paris-Est, ENPC/CEREVE, 77455 Marne-la-Vallee Cedex 2, France

thickness is highly variable and the crust-mantle density contrast is very large. By considering isostatic equilibrium, and using global gravity and topography data, we show that this thickness variability is the dominant contribution to the surface g_z spectrum over the range ≈100–1000 km. Using estimates of mantle properties (viscosity, thermal conductivity, thermal expansion coefficient, etc.), we show that the mantle contribution to the mean spectrum is strongest at ≈1000 km and is comparable to the variable crust thickness contribution. Overall, we produce a model which is compatible with both the observed (horizontal and vertical) density heterogeneity and surface gravity anomaly statistics over a range of meters to several thousand kilometers.

Keywords Geogravity · Geopotential theory · Fractals · Multifractals · Scaling

1 Introduction

1.1 Gravity as a Probe of the Earth's Interior: Gravity Anomalies and Depths to Sources

The Earth's gravity field is highly variable over a very wide range of spatial scales. There are two approaches which have been used to understand this. The most common has been to seek one to one (deterministic) relations between the fluctuations in surface gravity at a given scale and density anomalies at corresponding depths. In local or regional studies, this idea is commonly used to infer the depth to the source of gravity anomalies from the spectral peaks of surface gravity (e.g., Bullard and Cooper 1948; Spector and Grant 1970; Maus and Dimri 1996); the methods of wavelet analysis represent the most recent development in this type of application (e.g., Fedi et al. 2005). The second (neglected) approach has aimed at understanding and explaining the overall scale dependence of the statistics and the relations between the rock density and surface gravity statistics. Both approaches exploit a basic result of potential theory which shows that the contribution to the surface gravity at horizontal wavenumber K decays exponentially with the depth of the layer.

Globally, the deterministic approach has attempted to interpret the separation of the density heterogeneities from different rheological layers—the lithosphere, asthenosphere, lower mantle, and core in order to understand the relationship between geodynamic processes and planetary gravity fields (see Bowin 2000 for a recent review). Figure 1 shows the Earth geoid up to 360th order (the EGM96 model, Lemoine et al. 1998), indeed it is plausible that the breaks at scales corresponding to ≈3000 km and to ≈100–200 km can be associated with the depths of core-mantle and mantle-crust boundaries. That the break at 100–200 km is indeed the reflection of the crust-mantle boundary with the mechanism of isostatic compensation can be confirmed by the comparison of the gravity and topography power spectra (Fig. 1). For uncompensated topography, the two spectra must be parallel (as they appear to be at high wave numbers). If the topography is completely compensated, the low wavenumber gravity power spectrum will be attenuated depending on the depth of compensation. The exact wavenumber where the break occurs depends on the flexural rigidity. The topography for wavenumbers $<(200\ \text{km})^{-1}$ (see Sect. 3.5) is apparently

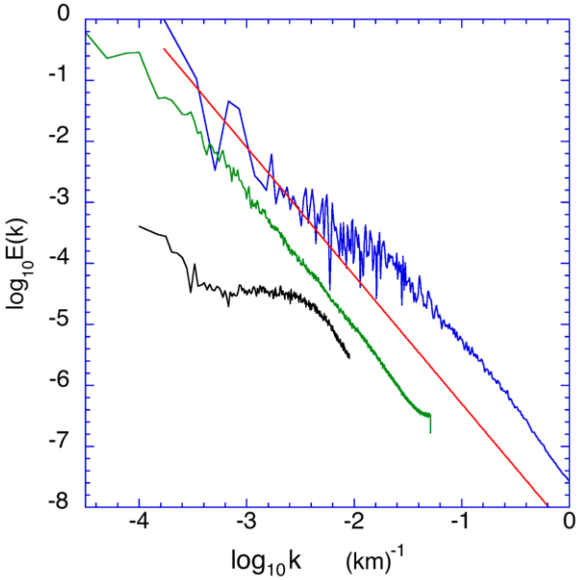

Fig. 1 Comparison of the surface gravity spectrum (*bottom*, shifted vertically for ease of comparison) with the ETOPO5 topography spectrum (*middle*) and continental US (*top*, two strips, each 512 × 65526 pixels long, each pixel, 90 m, also shifted vertically for clarity). *The red reference line* has slope -2.1. Wave number units: km^{-1}. *Black*, *lower left* shows the (isotropic) (spherical harmonic) global surface gravity spectrum calculated from the data discussed in Lemoine et al. (1998). The modes 1, 2 have been excluded, since they go far off-scale. The extreme high frequency ($k = 360$) corresponds to $\approx$100 km

fully compensated, whereas for wavenumbers $>(100\ \mathrm{km})^{-1}$–$(200\ \mathrm{km})^{-1}$ it is not. The actual break varies locally depending on flexural rigidity. Finally, the break at $\approx$3000 km in Fig. 1 could be a manifestation of the mantle core discontinuity. A final note before continuing: we use the terms “crust” and “mantle” somewhat loosely; we recognize that in many cases the terms “lithosphere” and “asthenosphere” might be more technically exact.

1.2 Geophysical Scaling and Surface Gravity

The deterministic approaches have been most successful in determining characteristic scales—either of rheological transitions, or of the depths of anomalies. They give no information about—nor understanding of—the statistics as functions of scale between the break points, nor information about the statistics of strong anomalies at fixed scales. In order to understand the observed wide range variability, some scaling (scale invariant) type assumptions are virtually mandatory since otherwise a (largely ad hoc) hierarchy of individual (nonscaling) sources of variability would have to be invoked every factor of 2 or 3 in scale. Indeed, there have been scaling models in solid earth geophysics ever since Vennig-Meinesz (1951) suggested that the energy[1]

---

[1] This is the (horizontal) angle integrated spectrum not the angle averaged spectrum; see discussion below.

at horizontal wave number K in the topography spectrum follows

$$E(K) \approx K^{-\beta_{\mathrm{top}}} \tag{1.1}$$

with $\beta_{\mathrm{top}} = 2$. Figure 1 shows that even with modern data Venning-Meinesz's spectrum is still an excellent approximation even down to scale below 1 km (although $\beta_{\mathrm{top}} \approx 2.1$, see Gagnon et al. 2003, 2006). If we perform isotropic scale reductions by a factor λ such that horizontal vectors are transformed as $\underline{X} \to \lambda^{-1}\underline{X}$, then the corresponding wave vectors are transformed as $\underline{K} \to \lambda\underline{K}$; we see that the power law form of $E(K)$ is conserved (it is "scaling"); the exponent β is "scale invariant". Spectra of this form are therefore expected if the underlying dynamical processes are also symmetric with respect to isotropic scaling transformations (systems symmetric with respect to such isotropic scaling transformations are called "self-similar").

The implications of the scaling of the topography for the gravity field have also been considered for some time. Kaula (1963) noted that the spectrum of the Earth's geoid follows a power law of the type (1.1) but with $\beta_{\mathrm{geoid}} \approx 3$. Since $\beta_{\mathrm{geoid}} = \beta_g + 2$, and over the range 200–3000 km Fig. 1 shows a flat gravity spectrum ($\beta_g \approx 0$), a value $\beta_{\mathrm{geoid}} \approx 2$ is more realistic. Kaula already noted that the power spectrum of the gravity potential due to uncompensated surface topography should have $\beta_{\mathrm{geoid}} = 4$, corresponding to a much more rapid decay than that observed. The discrepancy reflects the fact that the surface topography is by and large isostatically compensated.

Although studies of the scaling properties of rock density do not cover the same range of scales as those of gravity or topography, they have also tended to support the idea that various rock properties are scaling over wide ranges. For example, several recent (1-D) studies (Leary 1997; Pilkington and Todoeschuck 1993; Shiomi et al. 1997; Marsan and Bean 1999) have shown the rock density in boreholes to be scaling over the range ≈2 m to ≈1 km. The discovery of such empirical scalings have encouraged Maus and Dimri (1995, 1996), Maus (1999) to explore the consequences for the surface gravity implied by assuming self-similar (isotropic, unstratified) scaling rock density fields; their basic result is $\beta_g = \beta_\rho + 2$, where β_ρ is the exponent of the 3-D isotropic rock density spectrum.

1.3 Anisotropic Scaling, Geomagnetism, Geogravity

The assumption of isotropic rock density statistics is quite unrealistic if only because it contradicts the obvious fact of geological stratification. This anisotropy has been noted and quantified for the magnetic susceptibility by Pilkington and Todoeschuck (1995), and—more extensively—for various different physical properties (including density) by Leary (1997, 2003) who compared the spectra of horizontal and vertical boreholes. These authors (and recently Tchiguirinskaia (2002) for hydraulic conductivity in both the vertical and horizontal) made the important point that the scaling is obeyed in both horizontal and vertical directions, but with different exponents in the different directions. In Lovejoy and Schertzer (2007), we review these and other scaling properties of intensive quantities such as rock density, magnetic susceptibility, etc.

If the statistics in the horizontal and vertical directions are both scaling but different, then the overall system will be symmetric with respect to a scale change more general than isotropic reductions. The general formalism for handling scaling transformations is Generalized Scale Invariance (GSI; Schertzer and Lovejoy 1985a, 1985b). GSI shows that scale invariance is a (nonclassical) dynamical symmetry principle; as usual with symmetries, they are expected to hold in the absence of symmetry breaking mechanisms. A generic consequence of wide range GSI scaling is the existence of fractal structures with multifractal statistics; these features have now been reported in many areas of geophysics including the topography analyzed in Fig. 1 (Gagnon et al. 2003, 2006), and scaling has been proposed as a unifying paradigm for geodynamics (Schertzer and Lovejoy 1991; Lovejoy and Schertzer 1998). These papers also argued that the development of scaling models in geophysics has been held back because of the all too frequent reduction of scaling to the isotropic special case of self-similarity.

In a pair of papers (Lovejoy et al. 2001; Pecknold et al. 2001), we explicitly proposed that the Earth's magnetization (M) respects such an anisotropic scaling symmetry. Using potential theory and with the help of multifractal simulations of M and the associated surface magnetic field (B), we explored the consequences for the B field anomalies and the relationships between the M and B statistics. We have not only been able to reconcile stratified, anisotropic M scaling with the surface B scaling, but we have also showed that the anisotropy leads to a qualitatively new scaling regime which could explain the intermediate scale (100–2000 km scale) surface B statistics.

Our aim in this paper is to extend these results to gravity which—also being a potential field—has several similarities. For example, as with magnetism, an important success of anisotropic scaling models is evident at scales smaller than that of the crust thickness. This is because the isotropic (self-similar) relation between gravity and rock density spectral scaling exponents ($\beta_g = \beta_\rho + 2$) is untenable, since regional Bouguer gravity surveys have $\beta_g \approx 5$ (see Sect. 3.2.2) whereas empirically, $\beta_\rho \approx 1$ (see Sect. 3.2.1). However, since we show theoretically that[2] $\beta_g = \beta_\rho + 1 + H_z$ and the rock spectra indicate the anisotropy exponent $H_z \approx 3$, we will see that the small scale gravity exponent is correctly predicted by the theory and the rock density exponents.

Beyond these regional scales, the magnetism and gravity problems have important differences. For example, below the Curie depth (which is above the crust-mantle boundary), the magnetization vanishes whereas on the contrary, the corresponding gravity field has a source in the convective mantle. Although our information on the mantle density fluctuations is quite limited and indirect, a recent anisotropic scaling theory of high Prandtl number convection (Sect. 3.3) predicts that over the range from ≈20 to ≈3000 km the density should indeed respect anisotropic scaling (also with $H_z = 3$); we calculate the corresponding surface gravity statistics and compare them to the global gravity spectra. An additional difference between magnetism and gravity is that M does not appear to have a sharp discontinuity at the Curie depth so that the horizontal variation in the cut-off depth does not seem to generate a strong surface B anomaly. On the contrary, the density contrast at the crust-mantle boundary is large and is best modeled as a discontinuity across a (multi) fractal surface.

---

[2] This formula is valid if β_ρ is the horizontal density exponent and $H_z > 1$; see Sect. 3.

We do not consider scales larger than ≈3000 km, so that we ignore core and possible core-mantle boundary contributions. Although several of the present calculations are similar to those in the magnetism problem, by making a small change in our scale function ansatz, we are able to obtain many exact results and therefore can make precise comparisons between the gravity theoretically predicted from the density observations/models, and both global and regional surface gravity surveys. Although a full statistical characterization of the fields requires statistics of all orders for relative simplicity, we here limit ourselves to spectra (which are 2nd order). While for quasi Gaussian (e.g. monofractal) models these spectral results fully characterize the statistics, for multifractal models they only give a partial characterization.

This paper is structured as follows. In Sect. 2, we review the basic theory on anisotropic scaling and relevant results of potential theory and derive the connections between the second order rock density and surface gravity statistics (in both real and Fourier space). In Sect. 3, we apply the results to the crust and develop a scaling model of mantle convection as well as apply the result to the mantle and estimate the contribution to surface gravity of a scaling mantle-crust interface/topography model. In Sect. 4 we conclude.

2 Symmetries and the Relation between the Density and Gravity Fields

2.1 The Standard Density–Gravity Relations

In order to show how anisotropic scaling of the rock density field ($\rho(\underline{r})$) can lead to a scale break in the surface gravity (g_z) or gravitational potential (ϕ), first recall the solution of the Poisson equation

$$\underline{g} = -\nabla\phi; \qquad \phi(\underline{r}) = G\int \rho(\underline{r}')\frac{1}{|\underline{r}-\underline{r}'|}\,d\underline{r}', \tag{2.1}$$

where G is the universal gravitational constant. The convolution in the above can be regarded as a fractional integration of order 1; hence, if the problem (including the surface boundary conditions) were isotropic, the relative orders of singularity of the two fields (ρ, ϕ) would be simply shifted by one, leading to simple relations between the multifractal statistics of the two fields. However, the boundary conditions are clearly not isotropic, the classical assumption being that the rock is distributed over a half-volume bounded at $z = 0$. This amounts to ignoring the topography[3] and sphericity of the Earth. With this half-volume boundary condition, we obtain (e.g., Naidu 1968; Blakely 1995) the following particularly simple expression for the horizontal Fourier transform of the surface gravity

$$\tilde{g}_z(\underline{K}) = 2\pi G\int_0^\infty \tilde{\rho}(\underline{K}, z)e^{-zK}\,dz; \quad z \ge 0, \tag{2.2}$$

---

[3] Or, assuming that its effects can be removed/“corrected”.

the horizontal wavevector is $\underline{K} = (k_x, k_y)$, $K^2 = |\underline{K}|^2 = k_x^2 + k_y^2$, and $\tilde{\rho}(\underline{K}, z)$ is the horizontal Fourier transform of the density at depth z. We use the following convention for the D-dimensional Fourier transform pair $\tilde{f}(\underline{k})$, $f(\underline{x})$

$$\tilde{f}(\underline{k}) = \int_{-\infty}^{\infty} \tilde{f}(\underline{x}) e^{-\underline{k}\cdot\underline{x}} d^D\underline{x}; \qquad f(\underline{x}) = \frac{1}{(2\pi)^D} \int_{-\infty}^{\infty} f(\underline{x}) e^{i\underline{k}\cdot\underline{x}} d^D\underline{k}, \tag{2.3}$$

and also the convention that $z > 0$ downward. Equation (2.2) shows that the contributions of deep layers are exponentially attenuated. Defining the three-vector $\underline{k} = (\underline{K}, k_z)$, a more convenient equivalent expression is obtained in terms of the 3-D Fourier transforms $\tilde{\rho}(\underline{K}, k_z)$

$$\tilde{g}_z(\underline{K}) = 2\pi G \int_{-\infty}^{\infty} \tilde{\rho}(\underline{K}, k_z) \frac{dk_z}{-K + ik_z}. \tag{2.4}$$

If we now assume statistical translational invariance, then the various Fourier modes are statistically independent (2.6) and the horizontal spectral density is easily obtained by multiplying the above by the complex conjugate and ensemble averaging

$$P_g(\underline{K}) = 2(2\pi G)^2 \int_0^{\infty} \frac{P_\rho(\underline{K}, k_z)\, dk_z}{(K^2 + k_z^2)} \tag{2.5}$$

(the additional factor of 2 comes from the contributions for $k_z < 0$), and P_ρ, P_γ are the spectral densities of ρ, g_z

$$\langle \tilde{\rho}(\underline{k}) \tilde{\rho}(\underline{k}') \rangle = P_\rho(\underline{k}) \delta(\underline{k} + \underline{k}'); \qquad \langle \tilde{g}_z(\underline{k}) \tilde{g}_z(\underline{k}') \rangle = P_g(\underline{k}) \delta(\underline{k} + \underline{k}'). \tag{2.6}$$

Note that here and below, the symbol "$\langle\,\rangle$" denotes ensemble (statistical) averaging. We have used the symmetry $\tilde{f}(\underline{k}) = \tilde{f}^*(-\underline{k})$ (complex conjugate) valid when $f(\underline{x})$ is real.

If we now assume horizontal statistical isotropy, then the horizontal spectral density is a function only of K, and we define the isotropic energy spectrum ($E(K)$) by

$$E(\underline{K}) = 2\pi K P_g(\underline{K}); \quad K = |\underline{K}|. \tag{2.7}$$

The isotropic spectrum E is usually used in the turbulence literature; in isotropic systems it has the advantage that (contrary to P) it is independent of the space dimension (e.g., 1-D cross-sections will have the same E as for the full three-dimensional system; this is not true for P).

2.2 Anisotropic Scaling

Up until the 1980s, scaling was restricted to isotropic systems with unique fractal dimensions. Since then two generalizations have been important for geophysical applications: first, the treatment of statistics of all orders (not only second order), that is, multiscaling/multifractality, and second, the extension to anisotropic differentially stratified, and/or rotating systems, i.e., Generalized Scale Invariance (GSI, Schertzer and Lovejoy 1985a, 1985b). In the following, for simplicity we pursue the second order statistics. Our results will be valid for both anisotropic fractal and multifractal rock density models, although in the latter they will only provide a rather limited characterization of the statistics.

In order to understand GSI, it is helpful to introduce the dimensionless "scale function" $\|(\underline{X},z)\|$ which is the physically relevant notion of scale. The scale function satisfies the functional scale equation

$$\left\|T_\lambda(\underline{X},z)\right\| = \lambda^{-1}\left\|(\underline{X},z)\right\|, \tag{2.8}$$

where T_λ is the scale changing operator

$$T_\lambda = \lambda^{-G} \tag{2.9}$$

and G is the generator. The scale function is analogous to a norm, but need not respect the triangle inequality.[4]

In the special case where the statistics of the anisotropy independent of location (but not of scale), G is a matrix (linear GSI) and there exist conjugate Fourier space scale functions which satisfy

$$\left\|T_\lambda^T(\underline{K},z)\right\| = \lambda\left\|(\underline{K},z)\right\|, \tag{2.10}$$

where the "T" indicates the transpose (note the scale function in (2.10) is not generally the same as the real space counterpart which satisfies (2.8)).

If we have pure (scaling) stratification in the z direction, we may take the generator to be diagonal (this leads to self-affine statistics)

$$G = G^T = \begin{pmatrix} 1 & 0 & 0 \\ 0 & 1 & 0 \\ 0 & 0 & H_z \end{pmatrix} \tag{2.11}$$

(the first two rows/columns refer to k_x, k_y, the last to k_z), and an anisotropic spectral density may be written

$$P_\rho(\underline{K},k_z) = P_0\left\|(\underline{K},k_z)\right\|^{-s}, \tag{2.12}$$

where s is the spectral density exponent and P_0 is a constant determining the amplitude of the spectrum; if ρ is in $\mathrm{Kg\,m^{-3}}$, then P_0 is in $\mathrm{Kg^2\,m^{-3}}$. A convenient, but not unique, choice of $\|(\underline{K},k_z)\|$ is

$$\left\|(\underline{K},k_z)\right\| = \left(\left(\frac{K}{k_s}\right)^{H_z} + \frac{k_z}{k_s}\right)^{1/H_z}, \tag{2.13}$$

where we have introduced a "sphero-wave number" k_s at corresponding spheroscale $l_s = 2\pi/k_s$ (note that $K, k_s, k_z > 0$). At this scale, $P_\rho(k_s,0,0) = P_\rho(0,k_s,0) = P_\rho(0,0,k_s)$, i.e., P_ρ is roughly constant over a sphere; since $\|(k_s,0,0)\| = \|(0,k_s,0)\| = \|(0,0,k_s)\| = 1$, horizontal and vertical fluctuations have the same

---

[4] It need only define a series of decreasing balls, i.e., if $B_\lambda = T_\lambda B_1$ then $\lambda' > \lambda \Rightarrow B_\lambda \subset B_{\lambda'}$.

variance. Indeed, here and in the following, any scale function satisfying linear GSI (i.e., including those in which G has off-diagonal elements, as long as its eigenvalues are real[5]) will give essentially the same qualitative results (including for the gravity spectrum) as those discussed here.

Using the sphero-scale as a reference scale, dimensional analysis gives

$$P_0 = C\rho_s^2 l_s^3 = C\rho_s^2 (2\pi)^3 k_s^{-3}, \tag{2.14}$$

where ρ_s^2 is the density variance at the sphero-scale and C is a dimensionless constant which depends on the exact definition of ρ_s and of the unit ball.

2.3 Second Order Horizontal and Vertical Density Statistics. The Crust

The above choice of P_ρ (2.15), (2.16) determines the second order horizontal and vertical density statistics. The horizontal spectrum is

$$\begin{aligned} E_\rho(K) &= 2\pi K \int_0^\infty P_\rho(K, k_z)\, dk_z = A_{\rho x}\rho_s^2 k_s^{-1}\left(\frac{K}{k_s}\right)^{-\beta_x}; \\ \beta_x &= (s - H_z - 1);\ \ (\text{if } s > H_z) \end{aligned} \tag{2.15}$$

(if $s < H_z$, then there is a high wavenumber divergence; if we prevent the divergence by using a finite high frequency cut-off, then $\beta_x = -1$). Here and below, the dimensionless constants will be denoted by A (spectral), B (real space), C (other) and can, when necessary, be found by comparing the exact results in Tables 1, 2 with the corresponding formulae in the text (see Appendices A, B, respectively). The corresponding vertical spectrum is

$$\begin{aligned} E_\rho(k_z) &= 2\pi \int_0^\infty P_\rho(K, k_z) K\, dK = A_{\rho z}\rho_s^2 k_s^{-1}\left(\frac{k_z}{k_s}\right)^{-\beta_z}; \\ \beta_z &= (s - 2)/H_z;\ \ (s > 2) \end{aligned} \tag{2.16}$$

(if $s < 2$, then there is a high wave number divergence; using a finite high frequency cut-off, we obtain $\beta_z = 0$).

Although k_s is the sphero-wave number as defined by the spectrum P_ρ, we note that

$$\frac{E_\rho(k_z = k_s)}{E_\rho(K = k_s)} = \frac{\Gamma(\frac{2}{H_z})\Gamma(\frac{s-2}{H_z})(s - H_z)}{2H_z^2\Gamma(\frac{s}{H_z})}, \tag{2.17}$$

which is not exactly unity (for the empirical crust exponents, $s = 5.3$, $H_z = 3$, we obtain a ratio of 0.18; Γ is the usual gamma function). This fact points to the inherent inaccuracy of estimates of the sphero-scale obtained from 1-D spectra E (rather than from the spectral density P). We also note that here the elliptical dimension

---

[5] The case of complex eigenvalues involves an infinite number of rotations of structures as the scale is varied from 0 to ∞; it is probably not relevant to the vertical stratification problem. See Pecknold et al. (2001) for applications in surface magnetic anomaly mapping.

Table 1 A comparison of various density and gravity formulae assuming $s > H_z > 1$ (applicable to the crust), see Appendix A

Crust statistics		
	Spectra	Structure functions
Density, horizontal	$E_\rho(K) = C_c 2(2\pi)^4 \dfrac{H_z}{s-H_z} \rho_s^2 k_s^{-1} \left(\dfrac{K}{k_s}\right)^{1+H_z-s}$; $s > H_z$	$S_\rho(\underline{\Delta X}, 0) = \rho_s^2 \left(\dfrac{\Delta X}{l_s}\right)^{s-H_z-2}$
Density, vertical	$E_\rho(k_z) = \dfrac{C_c(2\pi)^4 \Gamma(\frac{2}{H_z})\Gamma(\frac{s-2}{H_z})}{H_z \Gamma(\frac{s}{H_z})} \rho_s^2 k_s^{-1} \left(\dfrac{k_z}{k_s}\right)^{(2-s)/H_z}$; $s > 2$	$S_\rho(0, 0, \Delta z) = B_{\rho z} \rho_s^2 \left(\dfrac{\Delta z}{l_s}\right)^{(\frac{s-2}{H_z})-1}$; $s - 2 > H_z$
Column integrated density fluctuation	$E_{I\rho}(K) = 2C_c(2\pi)^4 \rho_s^2 k_s^{-3} \left(\dfrac{k_s}{k_c}\right)^{1+s/H_z} \left(\dfrac{K}{k_s}\right)$; $K \ll k_s \left(\dfrac{k_c}{k_s}\right)^{1/H_z}$	$S_{I\rho}(\infty) = B_{I\rho}(2\pi)^2 \rho_s^2 k_s^{-2} \left(\dfrac{k_c}{k_s}\right)^{-(\frac{s-2}{H_z})-1}$
	$E_{I\rho}(K) = 2C_c(2\pi)^4 \rho_s^2 k_s^{-3} \dfrac{H_z+s}{H_z} \left(\dfrac{k_s}{k_c}\right) \left(\dfrac{K}{k_s}\right)^{1-s}$; $K \gg k_s \left(\dfrac{k_c}{k_s}\right)^{1/H_z}$	
Surface gravity	$E_g(K) = A_{gch} \rho_s^2 k_s^{-3} G^2 \left(\dfrac{K}{k_s}\right)^{-s}$; $K \gg k_s, H_z > 1$	$S_g(\Delta X) \approx \dfrac{A_{gch}}{8\pi^2} G^2 \rho_s^2 \dfrac{\Delta X^2}{s-3}$
	$E_g(K) = A_{gcl<} \rho_s^2 k_s^{-3} G^2 \left(\dfrac{K}{k_s}\right)^{-s/H_z}$; $s < H_z$; $K \ll k_s$	
	$E_g(K) = A_{gcl>} \rho_s^2 k_s^{-3} G^2 \left(\dfrac{K}{k_s}\right)^{-s-1+H_z}$; $s > H_z$	
Geoid	$E_{\mathrm{geoid}}(K) = \dfrac{E_g(K)}{g_z^2 K^2}$	$S_{\mathrm{geoid}}(\Delta X) \approx \dfrac{A_{gch}}{8\pi^2} \dfrac{G^2}{g_z^2} \rho_s^2 \dfrac{\Delta X^2}{s-1}$; $\Delta X < l_s$

$$B_{I\rho} = C_c \frac{4\pi \Gamma(\frac{2}{H_z})\Gamma(\frac{s-2}{H_z})}{(s-2+H_z)\Gamma(\frac{s}{H_z})}; A_{gch} = C_c \frac{(2\pi)^7}{2}; A_{gcl<} = C_c(2\pi)^7 \frac{\mathrm{Cos}(\frac{\pi}{2}(1-\frac{s}{H_z}))}{\mathrm{Cos}(\frac{\pi}{2}(1-\frac{2s}{H_z}))}; s < H_z; A_{gcl>} = C_c 2(2\pi)^6 \frac{H}{s-H_z}; s > H_z$$

Table 2 A comparison of various formulae for $s = H_z$ with an exponential high wave number cut-off at k_s and ρ_s as defined such that $R_{\rho m}(0,0,0) = \rho_s^2$ corresponding to the mantle convection model, see Appendix B. For the mantle model, take $H_z = 3$

Mantle statistics		
	Spectra	Structure functions
Density, horizontal	$E_\rho(K) \approx 2C_m(2\pi)^4\rho_s^2 k_s^{-2} K \log\left(\frac{k_s}{K}\right)^{H_z}$; $K \ll k_s$	$R_\rho(\underline{\Delta X}, 0) \approx 2H_z C_m \rho_s^2\left(\frac{l_s}{\Delta X}\right)^2$; $\Delta x \gg l_s$
Density, vertical	$E_{\rho z}(k_z) = C_m(2\pi)^4\left(\frac{2-H_z}{H_z^2}\right)\Gamma\left(\frac{2}{H_z}-1\right)\Gamma\left(1-\frac{2}{H_z}\right)\rho_s^2 k_s^{-1}\left(\frac{k_z}{k_s}\right)^{2/H_z-1}$	$R_{\rho z}(0,0,\Delta z) = B_{\rho z}\rho_s^2\left(\frac{l_s}{\Delta z}\right)^{2/H_z}$; $\Delta z \gg l_s$
Column integrated density fluctuation	$E_{I\rho}(K) = 2C_m(2\pi)^4\rho_s^2 k_s^{-3}\left(\frac{k_s}{K}\right)^2\left(\frac{k_s}{k_m}-1\right)$; $K > k_s\left(\frac{k_m}{k_s}\right)^{1/3}$ $E_{I\rho}(K) = C_m(2\pi)^4\rho_s^2 k_s^{-4} K\left(\left(\frac{k_s}{k_m}\right)^2-1\right)$; $K < k_s\left(\frac{k_m}{k_s}\right)^{1/3}$	
Surface gravity	$E_g(K) \approx \frac{4C_m(2\pi)^6 G^2\rho_s^2}{k_s^2 K}\log\left(\frac{k_s}{K}\right)$; $K \ll k_s$ $E_g(K) = 2C_m(2\pi)^6 G^2 k_s \rho_s^2 K^{-4}$; $K \gg k_s$ downward continuation distance z_c: $E_{gd}(K) = E_g(K)e^{-2Kz_c}$	$S_g(\underline{\Delta X}, 0) = 2C_m\left((2\pi)^2 G k_s^{-1}\rho_s\left(\log\left(\frac{k_s\Delta X}{2}\right)+\gamma_E\right)\right)^2$; $\Delta X \gg l_s$
Geoid	$E_{\text{geoid}}(K) = \frac{E_g(K)}{g_z^2 K^2}$	$S_{\text{geoid}}(\underline{\Delta X}, 0) \approx C_m\left(4\pi^2 G\rho_s k_s^{-1}\Delta X \log\frac{k_s}{k_m}\right)^2$; $\Delta X \gg l_s$

$H_z = 3$; $C_m = \frac{1}{(2\pi)^2\Gamma(\frac{2}{3})}$; $B_{\rho z} = C_m 2(2\pi)^{3-2/H_z} H_z^{-1}\cos\left(\frac{\pi}{H_z}\right)\Gamma\left(1-\frac{2}{H_z}\right)\Gamma\left(\frac{2}{H_z}\right)^2$

characterizing the rate of increase in volumes of typical structures[6] is $d_{\mathrm{el}} = 2 + H_z$. When $H_z = 1$, we obtain the isotropic value $d_{\mathrm{el}} = 3$, with the corresponding isotropic relation between exponents: $\beta_z = \beta_x = s - 2$.

It will also be convenient to express the statistics in real space via the correlation function (R) and structure functions (S). For statistically horizontally homogeneous systems these are defined by

$$\begin{aligned} R(\underline{\Delta x}) &= \langle f(\underline{x}) f(\underline{x} + \underline{\Delta x})\rangle, \\ S(\underline{\Delta x}) &= \langle (f(\underline{x}) - f(\underline{x} + \underline{\Delta x}))^2\rangle = 2(R(0) - R(\underline{\Delta x})). \end{aligned} \tag{2.18}$$

From the Wiener–Khintchin theorem we have

$$\begin{aligned} R(\underline{\Delta x}) &= \frac{1}{(2\pi)^D} \int_{-\infty}^{\infty} P(\underline{k}) e^{i\underline{k}\cdot\underline{\Delta x}}\, d^D\underline{k}; \\ S(\underline{\Delta x}) &= \frac{2}{(2\pi)^D} \int_{-\infty}^{\infty} P(\underline{k})(1 - e^{i\underline{k}\cdot\underline{\Delta x}})\, d^D\underline{k}. \end{aligned} \tag{2.19}$$

For the models discussed here, which are anisotropic in the vertical plane but isotropic in the horizontal, we have

$$\begin{aligned} R(0, 0, \Delta z) &= \frac{1}{\pi} \int_0^{\infty} \mathrm{Cos}(k_z \Delta z) E(k_z)\, dk_z; \\ S(0, 0, \Delta z) &= \frac{2}{\pi} \int_0^{\infty} (1 - \mathrm{Cos}(k_z \Delta z)) E(k_z)\, dk_z, \end{aligned} \tag{2.20a}$$

$$\begin{aligned} R(\underline{\Delta X}, 0) &= \frac{1}{(2\pi)^2} \int_0^{\infty} E(K) J_0(K\Delta X)\, dK; \\ S(\underline{\Delta X}, 0) &= 2 \int_0^{\infty} (1 - J_0(K\Delta X)) E(K)\, dK, \end{aligned} \tag{2.20b}$$

where $\underline{\Delta X} = (\Delta x, \Delta y)$ is a horizontal vector; $\Delta X = |\underline{\Delta X}|$ is the 2-D modulus and J_0 is the 0th order Bessel function.

Equations (2.15) and (2.16) have been derived by assuming that the scaling of P is respected for all K, k_z; see Appendix A for the effect of finite cut-offs (necessary, in particular, to account for the finite crust thickness). The constants $A_{\rho x}$, $A_{\rho z}$ have been chosen so that ρ_s^2 is the (horizontal) sphero-scale density fluctuation variance (structure function)

$$\begin{aligned} S_\rho(\underline{\Delta X}, 0) &= \rho_s^2 \left(\frac{\Delta X}{l_s}\right)^{\beta_x - 1}; \quad s > H_z, \\ S_\rho(0, 0, \Delta z) &= B_{\rho z} \rho_s^2 \left(\frac{\Delta z}{l_s}\right)^{\beta_z - 1}; \quad s > H_z + 2, \end{aligned} \tag{2.21}$$

---

[6] This type of spectrum was first proposed in the atmosphere Schertzer and Lovejoy (1985a) where the values $\beta_x \approx 5/3$, $\beta_z \approx 11/5$ (hence, $d_{\mathrm{el}} = 23/9 = 2.555\ldots$) were derived from dimensional analysis and confirmed by observation.

i.e., by definition of ρ_s, $S_\rho(l_s, 0, 0) = \rho_s^2$. Note that rather than defining the sphero-scale via the Fourier space k_s using $l_s = 2\pi/k_s$, one could define the sphero-scale in real space (l_{rs}) using, for example, $S_\rho(l_{rs}, 0, 0) = S_\rho(0, l_{rs}, 0) = S_\rho(0, 0, l_{rs})$. Since $B_{\rho z}$ is of order unity, the difference will generally not be large. However, if the β's are close enough to one (as is apparently the case in the crust), the difference can be large, see Appendix A. Here and throughout, we use the Fourier space definition $l_s = 2\pi/k_s$.

2.4 Second Order Horizontal and Vertical Density Statistics. The Mantle

The mantle model is discussed in Sect. 3.3, the spectrum is of the same general form as that discussed for the crust; hence, it is appropriate to discuss the corresponding gravity formulae here. Although the mantle and the crust formulae share the same basic anisotropic scaling form, there are nevertheless significant differences. For example, for the mantle $s = H_z (= 3)$, whereas for the crust $s > H_z$. This is significant, since when $s = H_z$ there must be a high wavenumber cut-off at the sphero-scale to assure convergence of the horizontal spectra, i.e., formula (2.15) is only valid for $K, k_z < k_s$. Physically, the convection model upon which the density scaling law is based breaks down for these scales, the corresponding Peclet number is less than one, convection becomes ineffective. The necessity of a large wavenumber cut-off poses a technical problem: What is the most realistic/and or mathematically tractable cut-off? A related problem is the definition of the sphero-scale fluctuation variance ρ_s^2. The model choices made in dealing with these issues are considered in Appendix B; they will alter the constants in the following by a factor of order unity (comparison of various models indicates that the factors may be as large as 4).

In the special case $s = H_z$, we have

$$E_\rho(K) \approx A_{\rho x} \rho_s^2 k_s^{-2} K \log\left(\frac{k_s}{K}\right)^{H_z}, \quad k \ll k_s, \tag{2.22a}$$

$$E_\rho(k_z) \approx A_{\rho z} \rho_s^2 k_s^{-1} \left(\frac{k_z}{k_s}\right)^{2/H_z - 1}, \quad k_z \ll k_s. \tag{2.22b}$$

Similarly, in real space

$$R_\rho(\underline{\Delta X}, 0) \approx B_{\rho x} \rho_s^2 \left(\frac{l_s}{\Delta X}\right)^2, \quad \Delta x \gg l_s, \tag{2.23a}$$

$$R_\rho(0, 0, \Delta z) \approx B_{\rho z} \rho_s^2 \left(\frac{l_s}{\Delta z}\right)^{2/H_z}, \quad \Delta z \gg l_s \tag{2.23b}$$

(for the mantle, put $H_z = 3$ in the above). The correlation (rather than structure) function is used, since the corresponding spectrum is an increasing function of horizontal wave number up to the cut-off so that R rather than S is a pure power law (see (2.19) for the relation between them). Following the discussion in Appendix B, the optimum choice is the exponential cut-off model with the definition of ρ_s such that $R_\rho(0, 0, 0) = \rho_s^2$; these choices were used in determining the theoretical constants in Table 2.

2.5 Symmetries, Symmetry Breaking, and the Gravity Statistics

We have seen that the gravitational potential ϕ is the convolution denoted "$*$" of density ρ with the Green's function $|\underline{r}|^{-1}$

$$\phi \propto \rho * \frac{1}{|\underline{r}|} \tag{2.24}$$

(2.1); however, the Green's function is symmetric with respect to scale changes with isotropic generator $\mathbf{G} = \mathbf{1}$

$$\frac{1}{|\lambda^{-\mathbf{G}}\underline{r}|} = \lambda\frac{1}{|\underline{r}|}; \quad \mathbf{G} = \begin{pmatrix} 1 & 0 & 0 \\ 0 & 1 & 0 \\ 0 & 0 & 1 \end{pmatrix}. \tag{2.25}$$

The result is that ϕ has broken symmetry. A direct calculation of the horizontal spectrum of the vertical component of gravity (with low frequency cut-off; k_c) gives

$$\begin{aligned} E_g(K) &= 2(2\pi)^3 G^2 K \int_0^\infty \frac{P_\rho(K, k_z)\, dk_z}{|(\underline{K}, k_z)|^2} = 2(2\pi)^3 G^2 K \int_0^\infty \frac{dk_z}{|(\underline{K}, k_z)|^2 \|(\underline{K}, k_z)\|^s} \\ &= 2(2\pi)^3 G^2 K \int_0^\infty \frac{dk_z}{(K^2 + k_z^2)[(K/k_s)^{H_z} + (k_z/k_s)]^{s/H_z}}. \end{aligned} \tag{2.26}$$

We now consider in turn the two cases $s \neq H_z$, $s = H_z$.

(i) $s > H_z$. For the crust ($s > H_z$, no high frequency cut-off) this yields

$$\begin{aligned} E_g(K) &= A_{gch}\rho_s^2 k_s^{-3} G^2 \left(\frac{K}{k_s}\right)^{-\beta_h}, \quad K \gg k_s, \\ E_g(K) &= A_{gcl}\rho_s^2 k_s^{-3} G^2 \left(\frac{K}{k_s}\right)^{-\beta_l}, \quad K \ll k_s, \end{aligned} \tag{2.27}$$

i.e., there are two distinct regimes with high and low wavenumber exponents β_h, β_l given by

$$\begin{aligned} &\beta_l = s + 1 - H_z, \quad s > H_z, \\ &\beta_l = s/H_z, \quad H_z > s > 1, \\ &\beta_h = s, \quad H_z > 1. \end{aligned} \tag{2.28a}$$

This result shows that the incompatibility of the anisotropic scaling of the density with the isotropic scaling of the gravitational Green's function produces a break at the sphero-scale.

The corresponding formulae for $H_z < 1$ are

$$\begin{aligned} &\beta_l = s - 2, \\ &\beta_h = s - 3 + H_z, \quad s > H_z, \\ &\beta_h = 2/H_z - 2, \quad s < H_z, \end{aligned} \tag{2.28b}$$

From (2.28a, 2.28b) we see that if $s > H_z$ then, for any H_z, $\beta_h - \beta_l = H_z - 1$. However, we shall see that the empirical rock density spectra constrain $s > 1$ and from Fig. 1 we see that all of the transitions have $\beta_h - \beta_l > 1$; so that anisotropic scaling with $H_z < 1$ cannot explain them. In addition, we will see that the empirical evidence is fairly clear that $\beta_x > \beta_z$ for various rock properties including density, implying $H_z > 1$ (see also the survey Lovejoy and Schertzer (2007). Final evidence that $H_z > 1$ is that $\beta_h \approx 5$, so that $H_z < 1$ would imply (2.28b) that $s \approx 8$, $\beta_x, \beta_z > 6$ which are much too large. In what follows, we shall concentrate on the parameter range $H_z > 1$ (in particular, the values $s = 5.3$, $H_z = 3$ give a reasonable fit to the high wavenumber rock and gravity spectra). Note that for $s > H_z > 1$, we have $\beta_l = \beta_{\rho x} + 2$ which provides a strong constraint on models, since the mantle regime ($(\approx 3000\ \text{km})^{-1} < k < (\approx 200\ \text{km})^{-1}$), has $\beta_g \approx 0$, and $\beta_{\rho x} \approx 1$. This rules out a simple linear GSI model for the crust/mantle transition. Finally, when $H_z = 1$ (isotropy), we recover the standard result $\beta_l = \beta_h = s = \beta_{\rho x} + 2 = \beta_{\rho z} + 2$.

(ii) $H_z = s$. For the mantle ($s = H_z = 3$), we obtain

$$E_g(K) \approx A_{gmx,l} \frac{G^2 \rho_s^2}{k_s^2 K} \log\left(\frac{k_s}{K}\right); \quad K \ll k_s, \tag{2.29a}$$

$$E_g(K) = A_{gmx,h} G^2 k_s \rho_s^2 K^{-4}; \quad K \gg k_s. \tag{2.29b}$$

Note that this formula ignores the downward continuation factor e^{-2Kz_c} necessary to take into account the fact that the mantle is at a depth z_c below the crust. The corresponding real space results are given in Table 2 and in Appendix B.

It is also of interest to calculate the corresponding formulae for the geoid. The relation of the geoid and gravity spectra is

$$E_{\text{geoid}}(K) = \frac{E_g(K)}{g_z^2 K^2}. \tag{2.30}$$

Corresponding formulae are given in Tables 1, 2 and Appendices A, B.

We have already noted that breaks in the gravity spectra introduced by the anisotropy of the rock density scaling cannot by themselves explain the shape of the gravity spectrum (Fig. 1) if only because the latter has two breaks. Since the effect of low wave number cut-off is not trivial, and an understanding is helpful in evaluating this and other (more realistic) models discussed in Sect. 3, we give details of the effect of a cut-off in Appendix A.

3 Scaling Models of the Density of the Crust, Mantle, Topography, and Interface

3.1 Discussion

In modeling the density of the crust-mantle system, we will need hypotheses about the topography, the crust-mantle spatial correlations and the nature of their interface; the latter being important because of the large (typically, $\approx 400\ \text{Kg}\,\text{m}^{-3}$) crust-mantle density contrast. Because of isostatic equilibrium, the crust-mantle interface and the topography contributions are intimately connected; (see Sect. 3.4). The spatial correlations between the crust and the mantle are most simply dealt with by considering them to be statistically independent systems. Physically, the most unrealistic consequence of this neglect of mantle "roots" of crustal structures is that it implies a strong statistical discontinuity in structure at the interface; however, since the interface will be treated as a (statistically independent) fractal discontinuity surface, this lack of statistical crust-mantle continuity may be less significant.

This model leads to the following equation (c.f. (2.2)) for the surface Fourier transform

$$\tilde{g}_z(\underline{K}) = \int_0^{z_c} \tilde{\rho}_c(\underline{K}, z) e^{-zK}\, dz + e^{-z_c K} \int_0^{z_m - z_c} \tilde{\rho}_m(\underline{K}, z) e^{-zK}\, dz, \qquad z \geq 0, \quad (3.1)$$

where crust and mantle parts are indicated with indices "c", "m", the crustal region is down to depth z_c, and the mantle between z_c and z_m. With the assumption of statistical independence of the crust and mantle (but also of Fourier components, (2.6)), we obtain

$$\begin{aligned} P_g(\underline{K}) = \langle |g_z|^2 \rangle \approx \int_{k_c}^{\infty} \frac{[P_c(\underline{K}, k_z) + e^{-2Kz_c} P_m(\underline{K}, k_z)]}{K^2 + k_z^2}\, dk_z \\ + e^{-2Kz_c} \int_{k_m}^{k_c} \frac{P_m(\underline{K}, k_z)}{K^2 + k_z^2}\, dk_z, \end{aligned} \quad (3.2)$$

where the factor e^{-Kz_c} takes into account the fact that the mantle layer starts at a depth z_c, not at $z = 0$ and where we have more convenient step-function Fourier space cut-offs: $k_c \approx 1/|z_c|$, $k_m \approx 1/|z_m - z_c| \approx 1/|z_m|$ (i.e., take $z_m \gg z_c$). Equation (3.2) shows how the crust and mantle contributions to the surface gravity may be combined.

3.2 The Crust

3.2.1 *Empirical Estimates of Model Parameters*

Unfortunately, very few data exist on spectral exponents for the rock density. Leary (1997) has probably the most extensive analyses with both horizontal and vertical spectra from similar regions. Due to strong (presumably multifractal) intermittency/variability (see Marsan and Bean 1999; Pecknold et al. 2001) individual boreholes have a fair amount of spectral variability (recall that the spectrum is an ensemble averaged quantity; the scaling is almost surely violated on every individual realization).

Before proceeding, it is useful to invert the relations (2.15)–(2.16) to obtain

$$H_z = \frac{(\beta_x - 1)}{(\beta_z - 1)}, \quad (3.3)$$

which is a convenient formula for estimating H_z from spectra.

The difficulty in estimating H_z (and the sphero-scale) is that Leary's results give roughly $\beta_z \approx 1$, $\beta_x \approx 1$; his precise analysis of 45 spectra (30 vertical, 15 horizontal) yields $\beta_z \approx 1.1 \pm 0.12$, $\beta_x \approx 1.34 \pm 0.12$, yielding $H_z \approx 3$ (the nearest integer). A comparable value ($H_z \approx 2$–3) was obtained for the magnetization (M) (Lovejoy et al. 2001; Pecknold et al. 2001); in obvious notation, if $H_{zM} = H_{z\rho}$ and $s_M = s_\rho$, then a statistical version of Poisson's relation may hold.[7] The spectrum from the much longer KTB borehole yields: $\beta_z \approx 1.2$ Lovejoy and Schertzer (2007); similarly, Shiomi et al. (1997) obtains $\beta_z \approx 1.1$–1.3 for sedimentary, $\beta_z \approx 1.3$–1.6 for volcanic rock. Finally, we should note that Leary also gives nearly identical values for the exponents for gamma decay and sound velocity; this supports the idea that the value of H_z (and hence d_{el}) may be the same for different physical properties and hence supports the notion that it may be a fundamental characteristic of the geological stratification.

The poor estimates of H_z (due to their small horizontal/vertical difference) lead to great uncertainty in estimating the sphero-scale. It can be roughly estimated using Leary's spectra (which are over the range ≈ 1–10^3 m), by extrapolating the horizontal and vertical spectra to their crossing point (although he gives exponents for 45 spectra, he only shows a single horizontal and a single vertical density spectrum). For the above exponents, this gives a crude estimate of the sphero-scale to be[8] ≈ 100 km, but this value is very sensitive to the exact values of β_x, β_z. In order to improve the reliability of this estimate and to use Shiomi's (vertical only) density spectra, we first graphically estimated the prefactors in the formulae $E_\rho(k_z) \approx E_{0z} k_z^{-1.1}$, $E_\rho(K) \approx E_{0x} K^{-1.3}$; these are shown in the table below where the units are rad m^{-1} for k, $\mathrm{Kg}^2\,\mathrm{m}^{-5}$ for E (Shiomi obtained an exponent of 1.27, but this is not too different from the 1.1 value from Leary). Shiomi normalized his densities by an unknown mean; from the graph of his borehole data, we estimated a mean density of $\rho_0 = 2.5 \times 10^3\ \mathrm{Kg\,m^{-3}}$, and used his graph to estimate the $E_{0\rho z}$ in Table 3.

The second step in obtaining a reliable estimate of ρ_s, k_s, was to use the DNAG Bouguer gravity data (Fig. 2). These anomalies were from 8 continental regions in North America; the compilations were made for the Decade of North American Geology (DNAG); resolution ≈ 5 km, 1024×1024 pixels. We note that the high wave number regime, down to 10^{-4} rad m^{-1} or so, is fairly linear on a log-log plot with slope $s \approx 5.3$ as predicted by the high frequency gravity (approximately given by $E_g(K) = C_h \rho_s^2 k_s^{-3} G^2 (\frac{K}{k_s})^{-s}$). In this power law regime, we estimate $E_g(K) \approx E_{0g} K^{-5.3}$ with $E_{0g} = 3.0 \times 10^{-25}$. Using this high wave number gravity formula, this leads to $\rho_s^2 k_s^{2.3} = 2.0 \times 10^{-7}$ which can then be used as a constraint in the density spectrum (which also depends on k_s, ρ_s, see (2.15), (2.16)). Unfortunately, due to the low wavenumber cut-off, these theoretical formulae are

---

[7] Poisson's relation is between magnetic and pseudo-gravity potentials and should not be confused with Poisson's equation. More precisely, if M has a constant direction and is everywhere proportional to ρ then both Poisson's relation and $H_{zM} = H_{z\rho}$ and $s_M = s_\rho$ follow. However, the latter does not necessarily imply the former.

[8] For comparison for gamma emission, we obtain ≈ 1 m, whereas for the velocity we find ≈ 1 km, but these are all quite inaccurate. In addition, for magnetic susceptibility, Lovejoy et al. (2001) estimate a sphero-scale at $\approx 10^4$–10^5 km.

Table 3 A comparison of various parameters estimated for the density field using the constraint from the DNAG gravity that $E_g(K=10^{-4}\ \mathrm{rad\,m}^{-1})=5\times10^{-4}\ \mathrm{m}^3$ (and crust thickness = 80 km, but the result is not too sensitive to this, see Fig. 2)

	E_0[b]	k_s (rad m^{-1})	l_s (km)	ρ_s (Kg m^{-3})	$\rho_s l_s$ (Kg m^{-2})
Shiomi et al. (1997)[a] (vertical)	1.17×10^4	$10^{-4.5}$	250	233	5.8×10^7
Leary (1997) (vertical)	1.92×10^4	$10^{-4.7}$	310	300	9.5×10^7
Leary (horizontal)	2.3×10^3	$10^{-4.3}$	125	113	1.4×10^7
Overall		$10^{-4.5}$	250	215	5.4×10^7

[a] For the Shiomi relative density fluctuations, we assumed a mean density $\rho_0=2.5\times10^3$ Kg m^{-3}

[b] These values assume $E=E_0k^{-\beta}$ with $\beta=\beta_x=1.3$ (horizontal), $\beta=\beta_z=1.1$ (vertical), and units of k in rad m^{-1}, units of E in Kg^2 m^{-5}

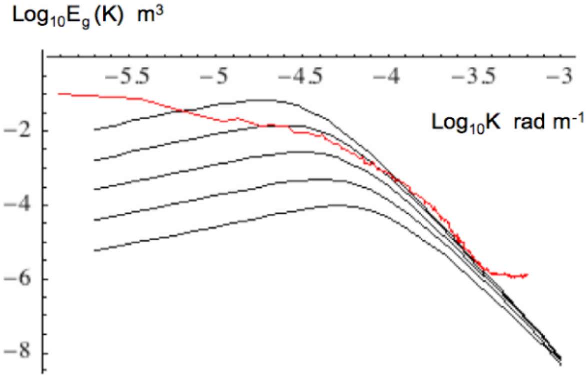

Fig. 2 A comparison of the crust model thickness 10, 20, 40, 80, 160 km with the DNAG spectrum (from North American continental Bouguer data over an area ≈5000 km across). The parameters $\rho_s=215$ Kg m^{-3}, $l_s=250$ km have been adjust to fit the function at $K=10^{-4}$ rad m^{-1}, 80 km thick, and the Shiomi and Leary borehole density data as above. The latter curve agrees well with the gravity data up to $\log_{10}K\approx-4.5$, i.e., up to about 200 km. The model low wave number slope is $+1$, the high wave number slope $-s=-\beta_h=-s=-5.3$ (the intermediate wave number regime discussed in the text is not visible since $k_c>k_s$)

not too precise. However, numerics (assuming the crust thickness in the range 40–160 km, see Fig. 2 for the limited dependence on k_c) give the solutions in Table 3 for k_s, ρ_s the overall "best" values being $\rho_s=215$ Kg m^{-3}, $l_s=2\pi/k_s=250$ km, $l_s\rho_s=5.4\times10^7$ Kg m^{-2}. The fact that $k_s<k_c$ (the crust cut-off) means that ρ_s cannot be interpreted as the actual sphero-scale variance; it is simply a dimensional parameter. In passing, we may note that the assumption of self-similar rock scaling ($H_z=1$) is untenable, since the DNAG estimate $s\approx5$ for the surface gravity exponent would imply $\beta_x=\beta_z=5-2=3$ which is much to steep to be compatible with the borehole data; indeed, the difference is so large that we can probably safely rule out the use of self-similar models in explaining the high wave number surface gravity variability.

3.2.2 Crust Density and Gravity Spectra, Structure Functions (<300 km)

Figure 2 shows that with these parameters the measured horizontal and vertical rock density statistics up to scales of a kilometer can be extrapolated up to vertical scales comparable to the crust thickness and horizontal scales of at least the order of several hundred kilometers without contradicting the surface gravity spectra. We argue in Sect. 3.4 that the breakdown at the larger horizontal scales is due to the large contribution from the fractal crust-mantle boundary which dominates for scales >100–300 km rather than because of a break in the horizontal scaling of the rock densities. Indeed, since the crust contribution to surface gravity falls off at low wave numbers with $\beta_l = -1$ (see Fig. 2), the crust contribution to the spectrum rapidly becomes smaller than the contribution from the crust-mantle interface or mantle. From the gravity spectrum alone, we cannot rule out the possibility that the horizontal crust density scaling continues up to planetary scales. Using these parameters, we can numerically calculate the crust statistics; these are shown in Figs. 3a–d.

3.3 The Mantle

3.3.1 Theoretical Statistics Far from Boundaries

The basic starting point is the consideration of very large (most often considered infinite) Prandtl number convection ($Pr = \nu/\kappa =$ viscosity/diffusivity; typical values for the mantle yield 10^{24}). This implies that inertial terms are totally negligible (e.g., the Reynolds number $Re = vL/\nu \approx 10^{-19}$ for typical values $L = 3 \times 10^6$ m, $v = 10^{-8}$ m/s, $\nu = 3 \times 10^{17}$ m^{2}s^{-1}). The standard approach to mantle convection concentrates on either a) the boundary layer where most of the temperature drop occurs; one nondimensionalizes the equations with typical external lengths, temperature gradients, etc., or b) the linearized nondimensional equations which are used to estimate the critical Rayleigh number (Ra) for the onset of convection (the latter is typically estimated at 1000–2000; however, the Ra for the entire Mantle is probably $>10^6$ so that chaotic behavior (as found in high resolution numerical models) is expected.

Lovejoy et al. (2005) describe a turbulence-type approach which is expected to be valid far from boundaries within high Prandtl number convection with quasi-constant heat flux. The basic argument is that if we are interested in the statistics in the interior mantle region far from boundaries, then the type of statistics should not depend on the outer boundaries; our approach is analogous to that used to obtain the Kolmogorov spectrum in fully developed turbulence (the latter is also expected to be insensitive to the nature of the forcing and boundaries). The most satisfying way to derive the Mantle convection scaling laws is to start from the basic convection equations for the fluctuations around the conductive solutions (see, e.g., Busse 1989)

$$\nabla \cdot \underline{u} = 0 \quad \text{Incompressibility,} \tag{3.4}$$

$$\nu^{-1}\left(\frac{\partial \underline{u}}{\partial t} + \underline{u} \cdot \nabla \underline{u}\right) = -\frac{\nabla p}{\nu \rho_0} + \nabla^2 \underline{u} - \underline{g}\alpha\nu^{-1}T$$

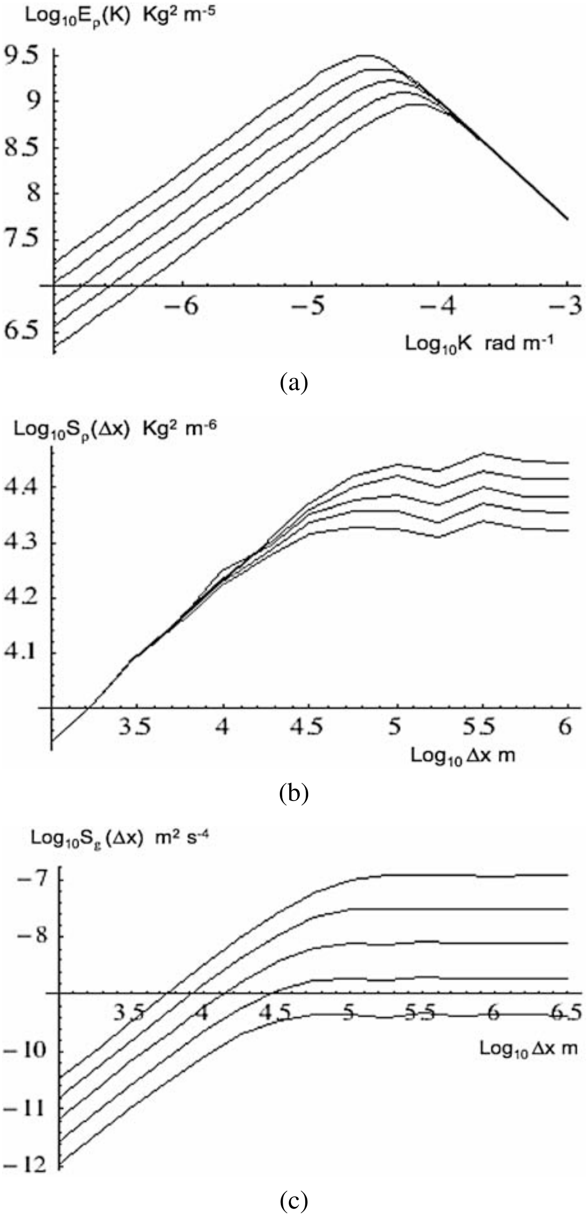

Fig. 3 (**a**) Horizontal density spectrum with crust thickness $2\pi/k_c = 10, 20, 40, 80, 160$ km, $l_s = 2.5 \times 10^5$ m, $\rho_s = 215$ Kg m^{-3}. The maximum is proportional to $(k_c/k_s)^{(1-s/H_z)}$; see Appendix A. (**b**) Horizontal density structure function $S_\rho(\Delta x)$ showing the variance of the density fluctuations as a function of separation distance Δx. The curves are for crust thickness 10, 20, 40, 80, 160 km, $l_s = 2.5 \times 10^5$ m, $\rho_s = 250$ Kg m^{-3}. The maximum is $\approx (k_c/k_s)^{(1+(2-s)/H_z)}$, see Appendix A: at 80 km it is about $(160 \text{ Kg m}^{-3})^2$. (**c**) The surface gravity structure function corresponding to (**b**) for $l_s = 2.5 \times 10^5$ m, $\rho_s = 215$ Kg m^{-3} and lithosphere thickness 10, 20, 40, 80, 160 km. $S_g = 10^{-10}$ m^{2}s^{-4} corresponds to 1 (mGal)^2. (**d**) The horizontal gravity spectra corresponding to $l_s = 2.5 \times 10^5$ m, $\rho_s = 215$ Kg m^{-3} and lithosphere thickness 10, 20, 40, 80, 160 km

Velocity equation (Boussinesq approx.), (3.5)

$$\frac{\partial T}{\partial t} + \underline{u} \cdot \nabla T = -\frac{\nabla \cdot \underline{H}}{c_p \rho_0} + \frac{J}{c_p \rho_0} + \frac{\nu_z Q}{\kappa c_p \rho_0} \quad \text{Temperature equation,} \tag{3.6}$$

$$\underline{H} = -\kappa \rho_0 c_p \nabla T + Q\hat{z} \quad \text{Heat diffusion equation,} \tag{3.7}$$

Fig. 3 (*Continued*)

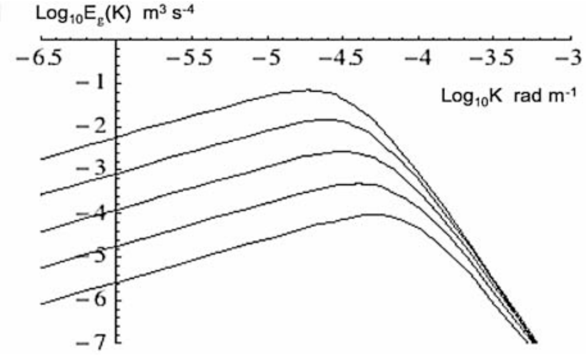

(d)

T, p are, respectively, the temperature and pressure differences with respect to a reference temperature and pressure (the solutions of the static equations), $\underline{H}$ is the heat flux, J is a volume heat source. We now ignore J with respect to the heat originating in the core, and take a typical value of $(\underline{H})_z = Q$, the vertical heat flux imposed by the bottom heating, top cooling. The v_z term in the Temperature equation arises because of the use of fluctuating T, as does the $Q\hat{z}$ term in the Heat diffusion equation ($Q\hat{z}$ is the vertical unit vector). Consider first the velocity equations (3.4), (3.5). Due to the very low Reynold's number we take $D\underline{u}/Dt \approx 0$ ("D/Dt" is the advective derivative). In addition, as usual the role of the pressure term is simply to maintain the incompressibility condition. Therefore, (3.5) depends only on the dimensionless combination $\frac{g\alpha}{\nu}$.

Considering the temperature equation, various arguments show that with the assumption on the imposed vertical heat flux boundary condition, that the main variations are in the z direction, i.e.,

$$v_z \frac{\partial T}{\partial z} \approx \frac{1}{c_p \rho_0} \frac{\partial (\underline{H})_z}{\partial z}. \tag{3.8}$$

Integrating over a layer and using a typical value of $(\underline{H})_z = Q$, this implies that only the combination of variables $\frac{Q}{c_p \rho_0}$ enters into the problem. Finally, we can note that the heat conductivity equation only contains the dimensionless combination $\kappa c_p \rho_0$.

We thus see that the dynamics depend on the three combinations: $\frac{g\alpha}{\nu}$, $\frac{Q}{c_p\rho_0}$, $\kappa c_p \rho_0$; since there are also three fundamental dimensions (temperature, distance, time), we obtain the unique dimensional quantities:

$$\begin{aligned} l_s &\approx \left(\frac{\rho_0 c_p \nu \kappa^2}{g\alpha Q}\right)^{1/4}, \\ \tau_s &\approx \left(\frac{c_p \rho_0 \nu}{Q g \alpha}\right)^{1/2}, \\ T_s &\approx \left(\frac{Q^3 \nu}{g\alpha \rho_0^3 c_p^3 \kappa^2}\right)^{1/4}. \end{aligned} \tag{3.9}$$

From these, we may derive a characteristic density and velocity

$$\begin{aligned} \rho_s &= \rho_0 \alpha T_s \approx \left(\frac{\alpha^3 \rho_0 Q^3 \nu}{g c_p^3 \kappa^2}\right), \\ v_s &= l_s/\tau_s. \end{aligned} \tag{3.10}$$

The significance of these numbers can be seen by considering the fluctuation Peclet number $Pe = \frac{l_s v_s}{\kappa}$ for fluctuations at scale l_s, velocity v_s. This dimensionless group characterizes the typical ratio of the dynamic heat transport terms to the heat diffusion terms. Using the above dimensional quantities, we obtain

$$Pe = \frac{l_s v_s}{\kappa} = 1, \tag{3.11}$$

i.e., for scales smaller than l_s, the heat transport is dominated by conduction, convection can be neglected, l_s is, therefore, the inner scale of the convection regime. We have used the subscripts "s" in anticipation of the fact that the inner scale is also a sphero-scale (see below).

Before continuing, we can note that using standard empirical estimates for the various parameters, we obtain quite reasonable values for l_s, v_s, ρ_s. In the final column, we give the combination $\rho_s l_s = (\frac{\alpha \rho_0 Q \nu}{g c_p})^{1/2}$, since according to (2.29a) (ignoring log corrections) this is the quantity that determines the mantle contribution to the surface gravity: To obtain the behavior of the statistics, we must perform a more detailed analysis of the equations. This may be done by considering the horizontal and vertical extent of convective plumes. In particular, it is possible to obtain two fundamental empirical laws relating the horizontal and vertical extent of laboratory generated plumes (C. Jaupard, private communication). If these laws are applied to an ensemble of plumes, the following anisotropic scaling results

$$\begin{aligned} \Delta T(\Delta x) &= T_s \left(\frac{\Delta x}{l_s}\right)^{-1}, \qquad & \Delta T(\Delta z) &= T_s \left(\frac{\Delta z}{l_s}\right)^{-1/3}, \\ \Delta v(\Delta x) &= v_s \left(\frac{\Delta x}{l_s}\right)^{1}, \qquad & \Delta v(\Delta z) &= v_s \left(\frac{\Delta z}{l_s}\right)^{1/3}, \end{aligned} \tag{3.12}$$

the density fluctuations may be obtained by multiplying the temperature equations by $\alpha \rho_0$. These equations justify the interpretation of l_s as the sphero-scale of the convection. Comparing this with (2.23), we see that $s = H_z = 3$. Physically, the decrease of temperature differences for points increasingly separated points (the negative exponents) seems reasonable, since it reflects the ability of the convection to better uniformize the temperatures over larger distances.

3.3.2 Mantle Parameters: Density, Gravity, Spectra, Structure Functions (>100 km)

We may see that (3.12) predict reasonable typical external velocities and temperatures. Taking the following values from Table 4, $T_s = 375$ K, $\rho_s = 30$ Kg m^{-3} and $l_s = 20$ km, $v_s = 2$ mm/yr, and defining λ as the scale ratio $\lambda = \frac{L}{l_s}$, where $L \approx 3000$ km is the thickness of the mantle and $l_s = 20$ km, we obtain $\lambda = 150$,

Table 4 The mean of the four estimates of $\rho_s l_s$ is 6×10^5 $\mathrm{Kg\,m^{-2}}$ which is the result that we use below (we also took $l_s = 20$ km, $\rho_s = 30$ $\mathrm{Kg\,m^{-3}}$, but as long as l_s is small enough, only the product is important at low frequencies)

	α	ρ_0	κ	c_p	Q	ν	l_s	v_s	T_s	ρ_s	$\rho_s l_s$
Quantity	Expansion coeff.	Density	Thermal cond.	Heat capacity	Thermal flux	Kinematic viscosity	Sphero-scale	Typical vertical velocity at l_s	Typical temp. fluct.	Typical density fluct.	Product
Units	$\mathrm{K^{-1}}$	$\mathrm{Kg\,m^{-3}}$	$\mathrm{m^2\,s^{-1}}$	$\mathrm{m^2\,s^{-2}\,K^{-1}}$	$\mathrm{Kg\,s^{-3}}$	$\mathrm{m^2\,s^{-1}}$	km	mm/yr	K	$\mathrm{Kg\,m^{-3}}$	$\mathrm{Kg\,m^{-2}}$
Poirier (1991)	3×10^{-5}	4×10^3	10^{-6}	10^3	8×10^{-2}	3×10^{17}	15.0	2.1	300	36	5.4×10^5
Jarvis and Pelletier (1989) (upper)	2×10^{-5}	3.7×10^3	1.5×10^{-6}	1.26×10^3	0.099	2.7×10^{17}	19.5	2.4	276	20.5	4.0×10^5
Jarvis and Pelletier (1989) (lower)	1.4×10^{-5}	4.7×10^3	2.5×10^{-6}	1.26×10^3	0.099	4.3×10^{17}	32.9	2.3	219	14.4	4.7×10^5
Overall	2×10^{-5}	4×10^3	1.5×10^{-6}	1.2×10^3	0.09	3.1×10^{17}	24	2	340	26	6×10^5

so that the typical temperature, velocity, density horizontal and vertical fluctuations with $\Delta x = \Delta z = 3000$ km are

$$\begin{aligned} &\Delta T(\Delta x) = T_s\lambda^{-1} \approx 2.5\ \mathrm{K}; && \Delta T(\Delta z) = T_s\lambda^{-1/3} \approx 70\ \mathrm{K}, \\ &\Delta v(\Delta x) = v_s\lambda \approx 45\ \mathrm{cm/yr}; && \Delta v(\Delta z) = v_s\lambda^{1/3} \approx 1.5\ \mathrm{cm/yr}, \\ &\Delta\rho(\Delta x) = \rho_s\lambda^{-1} \approx 0.5\ \mathrm{K}; && \Delta\rho(\Delta z) = \rho_s\lambda^{-1/3} \approx 6\ \mathrm{K}. \end{aligned} \tag{3.13}$$

This shows that at large enough scales, the free convection zone far from boundaries is indeed nearly isothermal (these values are fluctuations with respect to the static diffusive solutions of the equations). The typical vertical velocity horizontal shear of 45 cm/yr is also a rough estimate of the horizontal advection velocity at the top. Finally, we can consider the Rayleigh number (*Ra*) which must be high for convection. We obtain

$$Ra = \frac{g\alpha\Delta T\Delta z^3}{\nu\kappa} = \left(\frac{\Delta z}{l_s}\right)^{8/3}. \tag{3.14}$$

Using the largest scale $\Delta z = 3000$ km, $l_s = 20$ km, we obtain $Ra \approx 10^6$ which is comparable to but a little smaller than other estimates (see, e.g., the review in Jarvis and Pelletier 1989 where values 7×10^6–6×10^7 are suggested depending on the exact specification of the boundary conditions).

We can now use these values to calculate the second order surface gravity statistics; the main additional assumptions that are needed concern the details of the high wave number convection cut-off (these details are discussed in Appendix B and imply uncertainties of a factor of four or so). All the following mantle calculations use an exponential cut-off at the sphero-scale defined in real space at $l_s = 20$ km as the value for which $R(l_s, 0, 0) = \rho_s^2$. The upper bounds of the mantle are considered to be flat, lying directly underneath the crust (only the mantle contribution is shown); downward continuation to this depth is used; see Figs. 4a, b for the effect of varying depths to the top of the mantle. An additional assumption affecting the low wave number behavior is necessary at the lower bounds of the mantle. Since there is additional variability in the core, putting a drastic truncation at the wave number corresponding to the bottom of the mantle k_m would underestimate the true variability; hence, a cut-off corresponding to 6000 km rather than 3000 km was used. As seen in Fig. 5, this difference is only noticeable at the lowest wavenumbers.

The surface gravity field provides one of few ways of empirically testing the model; we therefore compared the theoretical predictions with both the global and DNAG spectra (Fig. 5). With the optimum parameters (Table 4), the figure shows that the contribution of the mantle to the surface gravity spectrum is barely discernable. However, in the next section we see that out to about $\log_{10} K \approx -5.7$ (i.e., 3000 km) that the surface gravity can be explained quite adequately by a fractal mantle-crust density discontinuity, so that this result is not surprising. Indeed, had the model predicted an effect larger even for a factor of only 4 or so, then the absence of a clear signature would have been difficult to explain. We should note that these conclusions are for ensemble averaged effects only; we may expect local regions to have somewhat larger mantle contributions to surface gravity, in these regions, a mantle gravity signature may be visible.

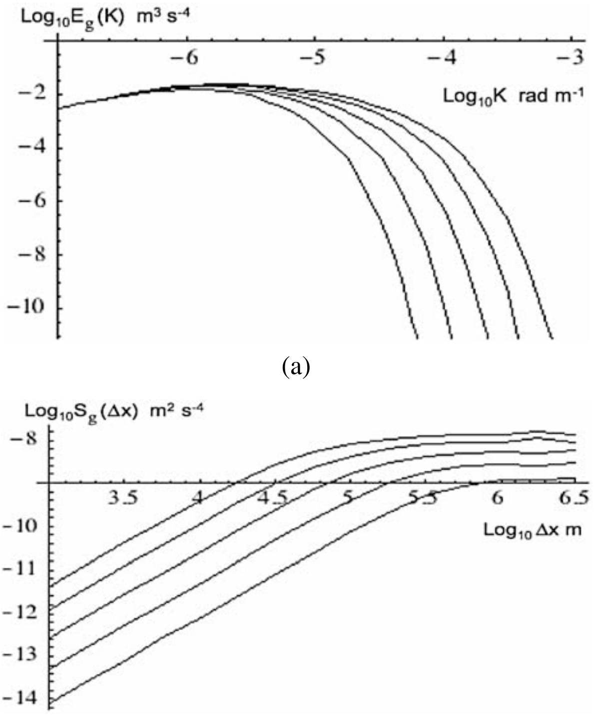

Fig. 4 (**a**) Mantle gravity spectrum the curves correspond to downward continuations of 10, 20, 40, 80, 160 km (*right to left*), $l_s = 20$ km, $\rho_s = 30\ \text{Kg}\,\text{m}^{-3}$. Mantle thickness is 6000 km, so as to partially account for the core. (**b**) Mantle gravity structure functions, $l_s = 20$ km, $\rho_s = 30\ \text{Kg}\,\text{m}^{-3}$, the curves correspond to downward continuations of 10, 20, 40, 80, 160 km (*top to bottom*)

(a)

(b)

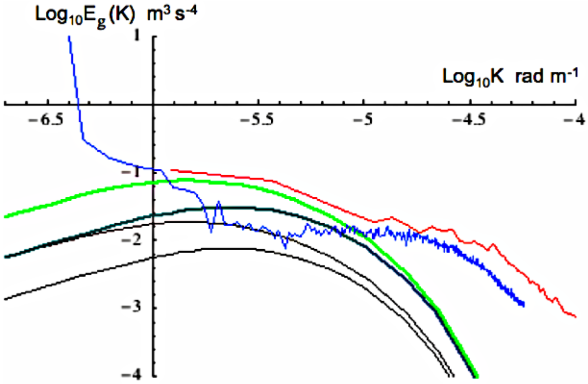

Fig. 5 Global and DNAG gravity (the *bottom*, *top empirical curves*, respectively), the thin theoretical curves are for the optimum estimates $\rho_s l_s = 6 \times 10^5$; the thick continuous curves are the corresponding curves for double this: $\rho_s l_s = 1.2 \times 10^6$. In each case, the upper curve is for mantle thickness 6000 km (to avoid an artificial drastic low wave number truncation), the lower for 3000 km. All four model curves assume a downward continuation of 80 km

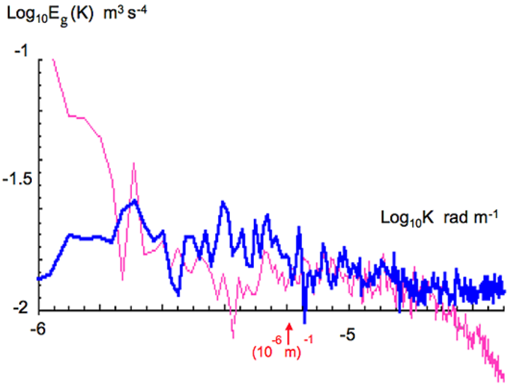

Fig. 6 Above: comparison of the global gravity spectrum (magenta), with that simulated from the global topography (*blue*) using the parameter $\Delta\rho_m^2 h_0^2 \chi^2 = 2.1 \times 10^{17}\ \mathrm{Kg\,m^{-2}}$. Putting in $\Delta\rho_m = 4 \times 10^2\ \mathrm{Kg\,m^{-3}}$, $h_0 = 100$ km, we obtain $\chi = 11$. The global gravity and that simulated from the topography agree over the range of 300–3000 km

3.4 Topography and the Crust/Mantle Interface Regime (≈300–3000 km)

Up until now, we have considered the Earth's surface as well as the mantle-crust boundary to be flat. However, Fig. 1 showed clearly that the topography is on the contrary scaling up to planetary scales, in addition processes of isostatic equilibrium imply that the variations in high wave number surface topography are associated with particularly deep "roots" (mantle-crust boundary depths). This suggests that we can use the observed surface topography as a statistical surrogate for the overall crust thickness if we assume that on average, the two are related by a numerical factor χ. The following derivation corresponds thus to the Airy model of isostatic equilibrium.

In order to determine the implications of varying crust thickness for the surface gravity, consider a crust with thickness varying as $h(\underline{R})$ where $\underline{R} = (x, y)$ is a surface position vector. This thickness takes into account the entire thickness of the crust (including the topography), except that all the corresponding mass is considered to reside in a column of uniform density $\rho(\underline{R}', z)$, and the top of the column is $z = 0$. The typical crust/mantle density contrast $\Delta\rho_m = \rho_m - \rho_c$ is about 400 $\mathrm{Kg\,m^{-3}}$ (=3300–2900). This uniform density approximation should not be too bad for scales comparable to or larger than the thickness. If we assume that the "roots" of the topography are χ times larger, then we have

$$h'(\underline{R}) = \chi h_t(\underline{R}), \tag{3.15}$$

where h_t is the altitude of the topography. Using this model (see Appendix D), we obtain:

$$E_g(K) \approx G^2 \Delta\rho_m^2 h_0^2 \chi^2 E_{h_t}(K) K^2; \quad K < 1/H, \tag{3.16}$$

i.e., in this range, $E_{h_t}(K) \propto E_{\text{geoid}}(K)$ (see (2.34)). h_0 represents a mean crust thickness about which the topography with "roots" represents a fluctuating part and $H > h_0$ is the thickest part of the crust encountered. Since $K \approx (1 - \exp(h_0 K))$ (see (2.2)), this formula is essentially the small K limit of a layer thickness h_0; we have ignored the flexural rigidity of the crust which—if fixed—would break the scaling; presumably a scaling rigidity model is required which is beyond our scope.

We can test out the implications of the above by comparing E_g with $K^2 E_{h_t}$. If the latter is multiplied by the factor $2.1 \times 10^{17}\ \mathrm{G}^2$ we obtain the excellent agreement indicated below over the range 300–3000 km. If $h_0 = 100$ km, this implies $\chi = 11$ which seems reasonable (see Fig. 6). We therefore conclude that such a fractal crust-mantle discontinuity surface can reasonably account for the surface gravity field all the way up to several thousand kilometers in scale.

3.5 Buoyancy Forces

One of the interesting properties of scaling models is the very long range of the implied correlations. In particular, fluctuations of column-integrated densities can be much larger than one would expect from classical (non scaling, Markov process type) statistical models. Horizontal variations in column integrated density will give rise to buoyancy forces; if these are large enough they could play a significant dynamical role. In Appendix C, we also obtain an analytic approximation to the maximum variance of the difference in column integrated densities. Using the empirical values of the constants (with $z_c = 80$ km), we estimate that for the crust the maximum standard deviation is the equivalent of about 100 m of rock (this occurs for distances of about $\Delta x = 170$ km). The corresponding numerically determined spectra and structure functions are shown in Figs. 7a, b. This is substantially smaller than the observed topographic variations, and is not likely to be an important effect. However a similar calculation for the mantle gives a much larger effect because of the much greater mantle thickness; in this case we estimate the maximum buoyancy force to be the equivalent of $\approx$1.5 km of rock (Figs. 7c, d). Since extremes may be several times larger (especially, since due to the likely multifractal nature of the density, we expect long or fat-tailed probability distributions), this may imply a direct role for mantle convection in orogenesis. Indeed, particularly large fluctuations–perhaps several times this value–might explain volcanic “hot spots”.

4 Conclusions

The recently published high resolution spectrum of the Earth’s geoid shows two breaks in the scaling at distances of roughly 3000 km and 100–200 km. The first clue to modeling the corresponding surface gravity field is to note that the contribution to the spectrum at horizontal wave number K decays exponentially with the depth of the source. These breaks are therefore naturally associated with fundamental changes in the Earth’s internal structure, i.e., with the thicknesses of the crust and mantle. While this classical explanation is valid as far as it goes, it can do no more than explain the characteristic scales of the breaks. A second clue to modeling the geoid is to note the ubiquity of the horizontal and vertical scaling of geophysical fields including the properties of the rocks (e.g., density, magnetization, radioactivity, seismic velocity). This suggests the use of scaling models; for scales smaller than tens of kilometers in the crust, this approach has been adopted by several researchers (e.g., Maus and Dimri 1995; Dimri and Vedanti 2005) and would follow if over wide ranges, the nonlinear dynamical processes responsible for the variability had no characteristic scale; they were scale invariant or “scaling”. The use of scaling models has the great advantage of automatically generating “red-noise” type scaling regimes similar to

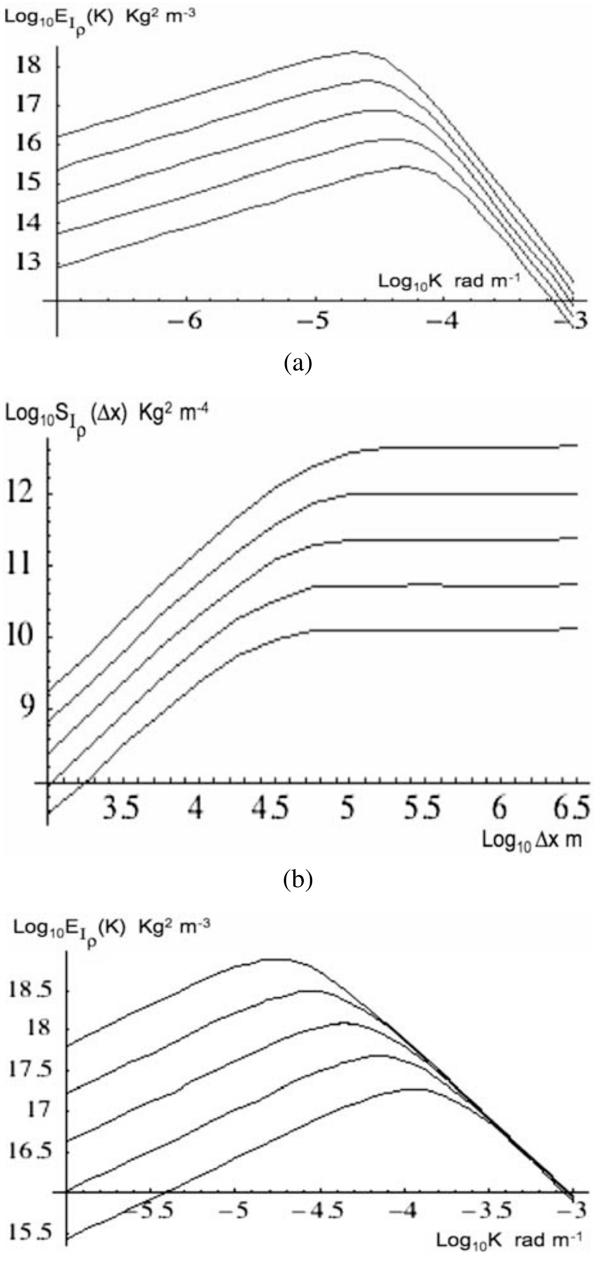

(a)

(b)

(c)

Fig. 7 (**a**) Spectrum of total column integrated density for $z_c = 10, 20, 40, 80, 160$ km (*bottom to top*) with $\rho_s = 250$ Kg m^{-3}, $l_s = 215$ km. (**b**) The structure function corresponding to $z_c = 10, 20, 40, 80, 160$ km with $\rho_s = 250$ Kg m^{-3}, $l_s = 215$ km. Using a mean lithosphere density of 3×10^3 Kg m^{-3}, the value $S_{I\rho} = 10^{11}$ Kg^2 m^{-4} corresponds to fluctuations of the order of 100 m of rock. The maximum at 160 km is $10^{12.4}$, i.e., about 500 m of rock. (**c**) Total vertically integrated fluctuations with $\rho_s = 30$ Kg m^{-3}, mantle thickness 3000 km, sphero-scale 10, 20, 40, 80, 160 km. (**d**) The structure function of the vertical integral of the rock density with mantle thickness = 3000 km with sphero-scale = $l_s = 10, 20, 40, 80, 160$ km, with $\rho_s = 30$ Kg m^{-3}. If $\rho_0 = 4 \times 10^3$ Kg m^{-3}, then the equivalent thickness of the rock is $\Delta z = (S_{I\rho}(\Delta x))^{1/2}/\rho_0$, i.e., 1 km of rock corresponds to $S_{I\rho} \approx 10^{13.2}$

that observed in boreholes. In addition, scaling processes have long range correlations, huge nonclassical fluctuations, they display potentially realistic anomalies at all scales. The first models of this type were isotropic, “self-similar”. However, as we showed in Sect. 2.3, the high variability (slow spectral fall-off, $\beta \approx 1$) in borehole

Fig. 7 (*Continued*)

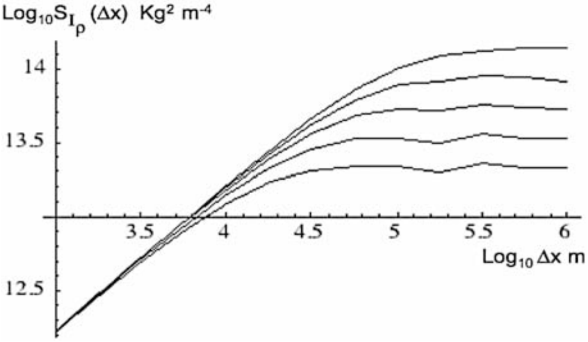

(d)

rock spectra and the corresponding low variability (rapid spectral fall-off, $\beta_h \approx 5$) of the small scale (<100 km) surface gravity are not compatible with self-similar (isotropic) models of rock density. A final flaw of the self-similar models is that they are not compatible with the observed horizontal/vertical stratification of the rocks.

Following the approach used in Lovejoy et al. (2001), Pecknold et al. (2001), Lovejoy and Schertzer (2007), we argue that while scaling is indeed a necessary ingredient in realistic models it must be anisotropic. Using a simple analytical model of the scaling spectrum, the first part of this paper (with various technical appendices) works out the consequences for second order statistics of the surface gravity field. In addition to the inner and outer breaks associated with any physical scaling regime, there is an additional source of scale breaking due to two incompatible symmetries, namely that of the isotropic gravitational Green's function (r^{-2} law for gravity) and the anisotropic rock density statistics. This introduces a scale break at the "sphero-scale" (l_s) where the density anomalies are roughly isotropic ("roundish").

We apply such anisotropic scaling models to both crust and mantle density fields. First, using (limited) borehole density data (from horizontal and vertical boreholes), combined with continental (Bouguer) gravity survey spectra, we estimate the fundamental exponents for the crust as $H_z \approx 3$, $s \approx 5.3$ and the sphero-scale at $l_s \approx 250$ km with the corresponding density fluctuations ≈ 215 Kg m^{-3}. Since $H_z > 1$ at scales smaller than l_s, the rocks will be increasingly stratified. This model can thus readily explain both the horizontal and vertical density statistics and the surface gravity anomalies up to 100–300 km.

We then considered the contributions to surface gravity coming from the mantle (important at larger scales). For this purpose we developed a theoretical model of rock density variations in the mantle. This model was based primarily on dimensional analysis of the equations of convection at high Prandtl and Rayleigh numbers, and predicts $H_z = s = 3$ and $\rho_s = 30$ Kg m^{-3}, $l_s = 20$ km. The mantle contribution to the (mean) surface gravity spectrum predicted by this model was of the same order, but somewhat smaller than the observed surface gravity spectrum at about 1000 km scales.

The final source of surface gravity that we consider arises from the large crust-mantle density contrast and the topography. Using a simple model combined with the ETPO5 global topography data (at $5'$ of arc), as a surrogate for the crust thickness

Table 5 The various exponents and values used in this paper. The mantle exponents are purely theoretical, ρ_s, $\rho_s l_s$ are from Table 4 whereas the crust values are purely empirical, most being obtained from Leary (1997) and Shiomi et al. (1997) density data with a single DNAG (Bouguer) gravity constraint

	H_z	s	l_s	ρ_s	$\rho_s l_s$
Mantle (from theory)	3	3	20 km	30 Kg m−3	6×10^5 Kg m^{-2}
Crust (from Leary and Shiomi data)	3	5.3	215 km	250 Kg m^{-3}	5.4×10^7 Kg m^{-2}

(corresponding to an assumption of Airy isostacy), we were able to quantitatively account for the surface gravity statistics over the range 300–3000 km.

The overall combined density/gravity model advocated here (see Table 5 for a summary, see Lovejoy et al. (2005) in the site www.physics.mcgill.ca/~gang/multifrac/index.htm for corresponding multifractal simulations) thus involves separate anisotropic scaling regimes for the mantle and crust separated by a fractal density discontinuity and seems capable of explaining the surface gravity statistics from scale of at least meters out to about 3000 km (where core/mantle boundary and core contributions are important). Since the mantle contribution to surface gravity was found to be smaller than that due to the fractal crust-mantle boundary, the overall model involved four internal parameters (H_z, s, l_s, z_c), and one additional external parameter (the crust/topography thickness ratio χ, see Table 5). Since the model predicts the second order statistical behavior of the density field in both horizontal and vertical directions, as well as the gravity spectrum, it is still fairly parsimonious. Although this study was deliberately confined to second order (spectral) statistics, the full scaling will likely show the density and the gravity to be multifractals (see Pecknold et al. 2001). They may enable us to make realistic multifractal models of the density and gravity.

Acknowledgements We especially thank J.C. Mareschal for numerous discussions and for support at various points in the project. We would also like to thank C. Jaupard, W. Peltier, M. Pilkington, J. Arkani-Hamed, and J. Toedeschuk for helpful discussions. This research was performed only for scientific purposes, it was unfunded.

Appendix A: Details of the Crust Density Formulae

A.1 The Basic Scaling of the Crust Density: Infinite Crust Thickness Results

For $H_z \neq s$, the horizontal spectrum is

$$E_\rho(K) = 2\pi P_0 K \cdot 2\int_{k_c}^{k_o} \frac{dk_z}{((\frac{K}{k_s})^{H_z} + \frac{k_z}{k_s})^{s/H_z}}$$
$$= -4\pi P_0 K \frac{H_z}{s - H_z} k_s \left(\left(\frac{K}{k_s}\right)^{H_z} + \frac{k_z}{k_s}\right)^{-s/H_z+1}\Bigg|_{k_c}^{k_o}, \qquad \text{(A.1)}$$

where k_c, k_o are the inner and outer crust scales (there is a factor of 2 for the negative k_z). Taking $k_c = 0$, $k_o = \infty$, we have

$$E_\rho(K) = C_c 2(2\pi)^4 \frac{H_z}{s - H_z} \rho_s^2 k_s^{-1} \left(\frac{K}{k_s}\right)^{1+H_z-s}; \quad s > H_z, \tag{A.2}$$

i.e., $\beta_x = s - H_z - 1$. Similarly, for the vertical spectrum

$$E_\rho(k_z) = 2\pi \int_0^\infty \frac{K\,dK}{((\frac{K}{k_s})^{H_z} + (\frac{k_z}{k_s}))^{s/H_z}}, \tag{A.3a}$$

$$E_\rho(k_z) = \frac{C_c(2\pi)^4 \Gamma(\frac{2}{H_z})\Gamma(\frac{s-2}{H_z})}{H_z \Gamma(\frac{s}{H_z})} \rho_s^2 k_s^{-1} \left(\frac{k_z}{k_s}\right)^{(2-s)/H_z}; \quad s > 2, \tag{A.3b}$$

i.e., $\beta_z = (s-2)/H_z$. We can calculate the (2-D) horizontal structure function using

$$S(\underline{\Delta X}, 0) = \frac{2}{(2\pi)^2} \int_0^\infty \big(1 - J_0(K\Delta X)\big) E(K)\,dK \tag{A.4}$$

and the (1-D) vertical structure function with

$$S(0, 0, \Delta z) = \frac{2}{\pi} \int_0^\infty \big(1 - \mathrm{Cos}(k_z \Delta z)\big) E(k_z)\,dk_z \tag{A.5}$$

(there is an extra factor of 2 from the integration from $-\infty$ to 0). Using $l_s = \frac{2\pi}{k_s}$ we obtain

$$S_\rho(\underline{\Delta X}, 0) = \rho_s^2 \left(\frac{\Delta X}{l_s}\right)^{s-H_z-2}, \quad s > H_z + 2 \tag{A.6}$$

(i.e., $S_\rho(\Delta X, 0) \propto \Delta X^{\beta_x - 1}$). If C_c is chosen to be equal to

$$C_c = \frac{\pi^{H_z-s}(s - H_z)\Gamma(\frac{s-H_z}{2})}{8H_z(-\Gamma(1 + \frac{H_z-s}{2}))} \tag{A.7}$$

then $S_\rho(l_s, 0, 0) = \rho_s^2$, i.e., ρ_s^2 is the sphero-scale fluctuation variance. Since there is a low wavenumber divergence, this is the only natural choice of reference scale for defining ρ_s. Putting $s = 5.3$, $H_z = 3$, we obtain $C_c = 8.66 \times 10^{-4}$. With this choice for C_c in (A.7), we obtain the following for the vertical structure function

$$S_\rho(0, 0, \Delta z) = B_{\rho z} \rho_s^2 \left(\frac{k_s \Delta z}{2\pi}\right)^{(\frac{s-2}{H_z})-1} = B_{\rho z} \rho_s^2 \left(\frac{\Delta z}{l_s}\right)^{(\frac{s-2}{H_z})-1}; \quad s - 2 > H_z \tag{A.8}$$

with the constant $B_{\rho z}$ given by

$$B_{\rho z} = C_c (2\pi)^{2+(\frac{s-2}{H_z})} \frac{\Gamma(\frac{2}{H_z})\Gamma(\frac{s-2}{H_z})\Gamma(\frac{s-2}{H_z} + 1)\sin(\frac{\pi}{2}(\frac{s-2}{H_z}))}{H_z \Gamma(\frac{s}{H_z})} \tag{A.9}$$

(i.e., $S_\rho(0,0,\Delta z) \propto \Delta z^{\beta_z - 1}$). Putting $s = 5.3$, $H_z = 3$, we obtain $B_{\rho z} = 0.124$. The fact that this dimensionless constant is not unity reflects the fact that the real space and Fourier space sphero-scales are not identical. Indeed, if we define the real space sphero-scale l_{rs} as the scale at which the vertical and horizontal structure functions are equal ($S(l_{rs},0,0) = S(0,l_{rs},0) = S(0,0,l_{rs})$), then we obtain

$$\frac{l_{rs}}{l_s} = B_{\rho z}^{\frac{1}{\beta_x - \beta_z}} \tag{A.10}$$

which with the above values, i.e., $\beta_x = 1.3$, $\beta_z = 1.1$, yields a ratio 2.96×10^{-5}. Using $l_s = 250$ km, this predicts $l_{rs} \approx 1$ m, but this value is so sensitive to the small difference $\beta_x - \beta_z$ that it should not be taken too seriously. In addition, this estimate does not take into account the finite crust thickness which will affect l_{rs} as determined by the structure functions as defined here (but will not affect l_s). However, the smallness of the difference does indicate that direct (real space) measurements of l_{rs} (from rock outcrops, for example) are thus likely to be highly variable.

A.2 The Effect of Finite Crust Thickness on Density and Gravity Statistics

The finite thickness of the lithosphere is important so that we must consider the case $k_c \neq 0$ (the results will be insensitive to the high wave number cut-off which we therefore put at ∞). For the horizontal density spectrum, from (A.1), we have

$$E_\rho(K) = 4\pi P_0 \frac{H_z}{s - H_z} k_s K \left(\left(\frac{K}{k_s} \right)^{H_z} + \frac{k_c}{k_s} \right)^{-s/H_z + 1}, \quad s > H_z. \tag{A.11}$$

With respect to the infinite lithosphere behavior, we see that there is a new $E_\rho(K) \approx K$ regime for $K < k_s (k_c/k_s)^{1/H_z}$.

For the corresponding horizontal structure function, there is no simple analytic expression, however, for the total variance

$$\begin{aligned} R_\rho(0,0,0) = \langle \rho^2 \rangle &= \int_0^\infty E_\rho(K)\, dK = \int_{k_c}^\infty E_\rho(k_z)\, dk_z \\ &= 2C_c (2\pi)^4 \rho_s^2 \left(\frac{k_c}{k_s} \right)^{1 + \frac{2-s}{H_z}} \frac{\Gamma(\frac{2}{H_z}) \Gamma(\frac{s-2}{H_z} - 1)}{H_z \Gamma(\frac{s}{H_z} - 1)}. \end{aligned} \tag{A.12}$$

This expression diverges as $k_c \to 0$ (explaining why we did not take ρ_s to be defined as the total variance). This determines the maximum of the density structure function.

The corresponding gravity spectrum is

$$\begin{aligned} P_g(K) &= (2\pi G)^2 2 \int_{k_i}^{k_o} P_\rho(K, k_z) \frac{dk_z}{K^2 + k_z^2} \\ &= 2(2\pi G)^2 \frac{P_{0c}}{K} \big(I_{s,H_z}(K, k_o) - I_{s,H_z}(K, k_i) \big), \end{aligned} \tag{A.13}$$

where for $s \neq H_z$

$$I_{s,H_z}(K,k_z) = \left(\tfrac{H_z}{s-H_z}\right)\operatorname{Im}\left[\tfrac{\|(K,k_z)\|^{H_z-s}}{\|(K,-iK)\|^{H_z}}\,{}_2F_1\left(\left(1-\tfrac{s}{H_z}\right),1,\left(2-\tfrac{s}{H_z}\right),\right.\right.$$
$$\left.\left.\tfrac{\|(K,k_z)\|^{H_z}}{\|(K,-iK)^{H_z}}\right)\right], \tag{A.14}$$

$${}_2F_1(a,b,c,z) = \tfrac{\Gamma(c)}{\Gamma(b)\Gamma(c-b)}\int_0^1 t^{b-1}(1-t)^{c-b-1}(1-tz)^{-a}\,dt$$

(the K^{-1} is used in the definition of I so as to make the latter dimensionless), where ${}_2F_1$ is the hypergeometric function with integral representation indicated. For the case $k_o = \infty$, and large K, we obtain the simple result independent of H_z, as long as $H_z > 1$,

$$\begin{aligned} I_{s,H_z}(K,\infty) &\approx \frac{\pi}{2}\left(\frac{K}{k_s}\right)^{-s}; \quad K \gg k_s, \\ I_{s,H_z}(K,0) &\approx O\left(\left(\frac{K}{k_s}\right)^{1-s-H_z}\log K\right); \quad K \gg k_s. \end{aligned} \tag{A.15}$$

Hence, for any $s > 0$, $H_z > 1$, the low k_z contribution is negligible, so that

$$E_g(K) = C_h \rho_s^2 k_s^{-3} G^2 \left(\frac{K}{k_s}\right)^{-s}, \quad K \gg k_s \tag{A.16}$$

with the dimensionless constant C_h, given by

$$C_h = \frac{C_c}{2}(2\pi)^7. \tag{A.17}$$

Using $s = 5.3$, $H_z = 3$, we obtain $C_h = 167$.

Using this formula to estimate the structure function of the surface gravity and geoid, integrating in the horizontal from high frequencies down to k_s, we obtain

$$\begin{aligned} S_g(\underline{\Delta X},0) &\approx \frac{C_h}{8\pi^2} G^2 \rho_s^2 k_s^{-2} \frac{(\Delta X k_s)^2}{s-3}; \quad \Delta X k_s < 1, \\ S_{\text{geoid}}(\underline{\Delta X},0) &\approx \frac{C_h}{8\pi^2}\frac{G^2}{g_z^2}\rho_s^2 k_s^{-2}\frac{(\Delta X k_s)^2}{s-1}; \quad \Delta X k_s < 1. \end{aligned} \tag{A.18}$$

In the case of gravity, the structure function saturates at distances a little larger than $\Delta x = l_s$; for the geoid it changes to another power law.

Also, for the low frequency regime, we obtain (to leading order)

$$I_{s,H_z}(K,\infty) \approx \pi \frac{\operatorname{Cos}(\frac{\pi}{2}(1-\frac{s}{H_z}))}{\operatorname{Cos}(\frac{\pi}{2}(1-\frac{2s}{H_z}))}\left(\frac{K}{k_s}\right)^{-s/Hz}; \quad K \ll k_s; \tag{A.19}$$

whereas

$$I_{s,H_z}(K,0) \approx -\frac{H_z}{s-H_z}\left(\frac{K}{k_s}\right)^{-s-1+H_z}; \quad K \ll k_s. \tag{A.20}$$

Hence, the contribution from large k_z dominates for $s < H_z$, while for $s > H_z > 1$ the small k_z contribution dominates. Overall, we obtain for the energy spectrum

$$\begin{aligned} E_g(K) &= C_l \rho_s^2 k_s^{-3} G^2 \left(\frac{K}{k_s}\right)^{-s/H_z}; \quad s < H_z, \\ E_g(K) &= C_l \rho_s^2 k_s^{-3} G^2 \left(\frac{K}{k_s}\right)^{-s-1+H_z}; \quad s > H_z,\ K \ll k_s, \end{aligned} \tag{A.21}$$

with the dimensionless constant C_l, given by

$$\begin{aligned} C_l &= C_c (2\pi)^7 \frac{\mathrm{Cos}(\frac{\pi}{2}(1-\frac{s}{H_z}))}{\mathrm{Cos}(\frac{\pi}{2}(1-\frac{2s}{H_z}))}, \quad s < H_z, \\ C_l &= 2C_c(2\pi)^6 \frac{H_z}{s-H_z}, \quad s > H_z. \end{aligned} \tag{A.22}$$

Using $s = 5.3$, $H_z = 3$, we obtain $C_l = 140$. Hence, for the parameters $H_z > s$, we obtain

$$\begin{aligned} \frac{E_\rho(K)}{E_g(K)} &= \frac{H_z}{2\pi^3(s-H_z)G^2} k_s^2 \left(\frac{K}{k_s}\right)^{1+H_z}; \quad K \gg k_s, \\ \frac{E_\rho(K)}{E_g(K)} &= \frac{K^2}{(2\pi)^2 G^2}; \quad K \ll k_s. \end{aligned} \tag{A.23}$$

For the case $H_z = s = 3$, see below. This shows clearly that for $H_z > 1$, the stratification does not affect the low wavenumber regime; while on the contrary, it totally determines the high wave number behavior.

In the case of the surface gravity, the finite cut-off at k_c leads to a third regime as outlined in Lovejoy et al. (2001) for the aeromagnetic case. This can be seen by defining the variable z

$$z = \frac{\|(K, k_c)\|^{H_z}}{\|(K, -iK)\|^{H_z}}. \tag{A.24}$$

We then have three regimes for $k_c > k_s$:

$$\begin{aligned} z &\approx 1; \quad K \gg k_s \left(\frac{k_c}{k_s}\right)^{1/H_z}, \\ z &\approx \frac{k_c}{k_c}\left(\frac{K}{k_s}\right)^{-H_z}; \quad k_s \left(\frac{k_c}{k_s}\right)^{1/H_z} > K > k_s, \\ z &\approx \frac{ik_c}{k_c}\left(\frac{K}{k_s}\right)^{-1}; \quad k_s < K. \end{aligned} \tag{A.25}$$

However, using the estimate $k_c/k_s \approx 3$ ($k_s = 2\pi/250$ km, $k_c = 2\pi/80$ km) we find that the middle regime (which has $k^{-(s-1)}$ behavior; see Lovejoy et al. 2001) holds over a mere factor of $3^{1/3}$ and is thus is too limited in range to be noticeable.

Appendix B: Details of the Mantle Density Statistics

B.1 The High Wavenumber Cut-Off

Contrary to the crust case with $s > H_z$, for the mantle, the convection model gives $s = H_z = 3$ which implies high wave number divergences. However, the sphero-scale plays the role of high wave number cut-off, with the result that many of the statistics are somewhat sensitive to the exact high wave number details. Given a model for the cut-off, a related problem is to find the most physically appropriate definition of the sphero-scale. In this appendix, we discuss both of these issues. The question of the cut-off will be illustrated by comparing two simple models.

(1) *Wavenumber truncation.* If we introduce a drastic cut-off in Fourier space at $k_z = k_s$, then we obtain the following horizontal density spectrum

$$E_\rho(K) = 2\pi P_0 K \cdot 2 \int_0^{k_s} \frac{dk_z}{(\frac{K}{k_s})^3 + \frac{k_z}{k_s}} = 2C_m (2\pi)^4 \rho_s^2 k_s^{-2} K \log\left(1 + \left(\frac{k_s}{K}\right)^3\right) \tag{B.1}$$

(the factor of 2 is from the integration over negative wave numbers); thus,

$$E_\rho(K) \approx 2C_m (2\pi)^4 \rho_s^2 k_s^{-2} K \log\left(\frac{k_s}{K}\right)^3; \quad K \ll k_s. \tag{B.2}$$

The above is the (log corrected) $\beta_x = -1$ behavior of the mantle convection theory. We can now calculate the total variance of the density fluctuations

$$\langle \rho^2 \rangle = R(0,0,0) = \frac{1}{(2\pi)^2} \int_0^{k_s} E_\rho(K)\, dK = 2C_m \rho_s^2 (2\pi)^2 \sqrt{3} \frac{\pi}{6}. \tag{B.3}$$

The drawback of this drastic Fourier space cut-off is that it is physically unrealistic, and mathematically it leads to a correlation function with artificial nonphysical oscillations about zero

$$\begin{aligned} R_\rho(\underline{\Delta X}, 0) &= \frac{1}{(2\pi)^2} \int_0^\infty E_\rho(K) J_0(K \Delta X)\, dK \\ &\approx \frac{2CK(2\pi)^2 \rho_s^2}{k_s \Delta X} J_1(k_s \Delta X); \quad \Delta X \gg k_s^{-1}. \end{aligned} \tag{B.4}$$

(2) *Exponential cut-off.* It is more physically realistic to use an exponential cut-off which is less drastic and has the additional advantage of involving a more realistic correlation function. For this model, we take the modified spectrum

$$P_\rho(K, k_z) = P_0 e^{-\|(K,k_z)\|^3} \left\|(K, k_z)\right\|^{-3}. \tag{B.5}$$

We thus obtain

$$E_\rho(K) = 4\pi P_0 K k_s \Gamma\left(0, \left(\frac{K}{k_s}\right)^3\right), \tag{B.6}$$

where $\Gamma(0,x)=\int_x^\infty t^{-1}e^{-t}\,dt$ is the incomplete Gamma function. For $K<k_s$, we have the following expansion

$$E_\rho(K)\approx 4\pi P_0 K k_s\left(-\gamma_E-\log\left(\frac{K}{k_s}\right)^3+\left(\frac{K}{k_s}\right)^3+\cdots\right), \tag{B.7}$$

where $\gamma_{E=0.57\ldots}$ is the Euler Gamma. Note that the leading behavior for small K is $K\log K^3$ which is identical to the result for the truncated high frequency spectrum, but the $-2\pi P_0 K k_s\gamma_E$ is new. Also,

$$R_\rho(0,0,0)=\langle\rho^2\rangle=\frac{1}{(2\pi)^2}\int_0^\infty E_\rho(K)\,dK=\frac{2P_0k_s^3\Gamma(\frac{2}{3})}{4\pi}. \tag{B.8}$$

We also have a more realistic (nonoscillating) correlation function

$$\begin{aligned}R_\rho(\underline{\Delta X},0)&=\frac{1}{(2\pi)^2}\int_0^\infty E_\rho(K)J_0(K\Delta X)\,dK\\&\approx 2H_zC_m\left(\frac{2\pi\rho_s}{k_s\Delta X}\right)^2=2H_zC_m\left(\frac{\rho_s l_s}{\Delta X}\right)^2;\quad \Delta X\gg k_s^{-1}\end{aligned} \tag{B.9}$$

(with $H_z=3$). This exponential cut-off probably gives us the best estimate of C_m.

B.2 The Definition of ρ_s

Given the cut-off model, there are three obvious choices of definition of ρ_s:

$$\begin{aligned}\rho_{s1}^2&=R_\rho(0,0,0),\\ \rho_{s2}^2&=R_\rho(l_s,0,0)=R_\rho\left(\frac{2\pi}{k_s}\right),\\ \rho_{s3}^2&=\left(\frac{\Delta X}{l_s}\right)^2R_\rho(\Delta X,0,0);\quad \Delta X\gg l_s.\end{aligned} \tag{B.10}$$

Depending on which we use, we obtain different constants C_m. $R_\rho(0,0,0)$ gives the physically significant total variance. The second and third definitions are not very different; they only differ because the power law behavior of the correlation function is only asymptotically exact. The main choice is between either of these or the first, with the difference arising because of the non abrupt cut-off in the variance at the sphero-scale (a Fourier space truncation will in fact have variance at scales $<l_s$ comparable to the exponential cut-off). We favor the first definition, since it seems more physically relevant; in any case the differences are not large as Table 6 indicates.

Appendix C: Column Buoyancy

The spectrum of the running vertical integral of the density responsible for the total column buoyancy force for a column thickness l_z is given by

$$P_{Il_z,\rho}(K,k_z)=\left|\int_0^{l_z}e^{ik_zz}\,dz\right|^2P_\rho(K,k_z), \tag{C.1}$$

Table 6 This table shows how two different definitions of ρ_s and different high wave number cut-offs affect the constant C_m. Since the exponential cut-off is probably more realistic, and physically $\rho_s^2 =$ total variance is more significant, we use the value $C_m = 0.0187$

	$\rho_{s1}^2 = R_\rho(0,0,0)$	$\rho_{s3}^2 = (\frac{\Delta X}{l_s})^2 R_\rho(\Delta X)$	$\frac{\rho_{s2}}{\rho_{s1}} = (\frac{R_\rho(l_s,0,0)}{R_\rho(0,0,0)})^{1/2}$
Exponential cut-off	$C_m = \frac{1}{(2\pi)^2\Gamma(\frac{2}{3})} = 0.0187$	$C_m = 1/6 = 0.166$	2.98
Truncation	$C_m = \frac{\sqrt{3}}{4\pi^3} = 0.0139$	$C_m = 0.25$	4.23

where the first term is modulus squared of the Fourier transform of the indicator function of the integration interval. This yields

$$P_{Il_z,\rho}(K,k_z) = \left(\frac{2\sin(\frac{k_z l_z}{2})}{k_z}\right)^2 P_\rho(K,k_z) = \frac{4\sin^2(\frac{k_z l_z}{2})P_0}{k_z^2((\frac{K}{k_s})^{H_z} + \frac{k_z}{k_s})^{s/H_z}}. \tag{C.2}$$

To calculate the horizontal spectrum of the vertical integral, we integrate as usual over the entire crust (due to a low frequency divergence, a low frequency cut-off is indeed necessary). We use for this the simplest Fourier truncation model at wave number $k_c = 2\pi/l_c$, $l_c =$ crust thickness

$$E_{Il_z,\rho}(K) = 4\pi K P_0 \int_{k_c}^{\infty} \frac{4\sin^2(\frac{k_z l_z}{2})\,dk_z}{k_z^2((\frac{K}{k_s})^{H_z} + \frac{k_z}{k_s})^{s/H_z}}. \tag{C.3}$$

If we integrate over the entire column, then $l_c = l_z$ and we obtain

$$E_{I\rho}(K) = 4\pi K P_0 \int_{k_c}^{\infty} \frac{4\sin^2(\frac{k_z\pi}{k_c})\,dk_z}{k_z^2((\frac{K}{k_s})^{H_z} + \frac{k_z}{k_s})^{s/H_z}}. \tag{C.4}$$

The sine factor is mostly important for $k_z < k_c$, but the latter wave numbers are cut-off anyway, hence it makes a small change to the results. For many calculations we can therefore use the following approximation

$$E_{I\rho}(K) \approx 4\pi K P_0 \int_{k_c}^{\infty} \frac{dk_z}{k_z^2((\frac{K}{k_s})^{H_z} + \frac{k_z}{k_s})^{s/H_z}}. \tag{C.5}$$

Note that the large distance bound on the structure function is

$$S_{I\rho}(\infty) = 2R_{I\rho}(0) = 2\langle\rho_I^2\rangle = \frac{1}{\pi}\int_{k_c}^{\infty} E_\rho(k_z)\frac{dk_z}{k_z^2}. \tag{C.6}$$

Using this approximation, we obtain the analytic result

$$\begin{aligned} S_{I\rho}(\infty) &= B_{I\rho}(2\pi)^2\rho_s^2 k_s^{-2}\left(\frac{k_c}{k_s}\right)^{-(\frac{s-2}{H_z})-1}, \\ B_{I\rho} &= C_c\frac{4\pi\Gamma(\frac{2}{H_z})\Gamma(\frac{s-2}{H_z})}{(s-2+H_z)\Gamma(\frac{s}{H_z})}. \end{aligned} \tag{C.7}$$

If we include the sine factors, the corresponding expression is the same as the above but with corrections involving hypergeometric functions; numerically, for $s = 5.3$, $H_z = 3$, the difference is a factor of 1.76 (see Fig. 7). Putting the high frequency cut-off at ∞, we obtain

$$\begin{aligned} E_{I\rho}(K) &= 2C_c(2\pi)^4\rho_s^2 k_s^{-3}\left(\frac{k_s}{k_c}\right)^{1+s/H_z}\left(\frac{K}{k_s}\right) \\ &\quad \times {}_2F_1\left(\frac{s}{H_z}, 1+\frac{s}{H_z}, 2+\frac{s}{H_z}, -\left(\frac{k_s}{k_c}\right)\left(\frac{K}{k_s}\right)^{H_z}\right); \quad s > -H_z. \end{aligned} \tag{C.8}$$

This has the following low and high wave number regimes

$$\begin{aligned} E_{I\rho}(K) &= 2C_c(2\pi)^4\rho_s^2 k_s^{-3}\left(\frac{k_s}{k_c}\right)^{1+s/H_z}\left(\frac{K}{k_s}\right); \quad K \ll k_s\left(\frac{k_c}{k_s}\right)^{1/H_z}, \\ E_{I\rho}(K) &= 2C_c(2\pi)^4\rho_s^2 k_s^{-3}\frac{H_z+s}{H_z}\left(\frac{k_s}{k_c}\right)\left(\frac{K}{k_s}\right)^{1-s}; \quad K \gg k_s\left(\frac{k_c}{k_s}\right)^{1/H_z}. \end{aligned} \tag{C.9}$$

Appendix D: Estimating the Contribution from the Crust/Mantle Interface, Topography

If we now consider the case $|(\underline{R}-\underline{R}')| > h(R')$, we have the following approximation to the Green's function in (2.1)

$$\begin{aligned} g_z(\underline{R}|\underline{R}') &\approx \frac{G\rho_c(\underline{R}')h(\underline{R}')^2}{2|(\underline{R}-\underline{R}')|^3}\left(1-\frac{3}{4}\left(\frac{h(\underline{R}')}{|(\underline{R}-\underline{R}')|}\right)^2+\cdots\right); \\ h(\underline{R}') &\ll \left|(\underline{R}-\underline{R}')\right|, \end{aligned} \tag{D.1}$$

where $g_z(\underline{R}|\underline{R}')$ indicates the gravity at the surface location $\underline{R}$ due to a column at $\underline{R}'$. We now use the same approximation on a column in the mantle (density ρ_m), assumed to lie between depths h and $h_m \gg h$. Using the same approximation, and summing the contribution from the crust and mantle, we obtain

$$g_z(\underline{R}|\underline{R}') \approx -\frac{G}{2|(\underline{R}-\underline{R}')|^3}\left(h(\underline{R}')^2\Delta\rho_m + h_m^2\rho_m\right), \quad h(\underline{R}') \ll \left\|(\underline{R}-\underline{R}')\right\|. \tag{D.2}$$

The fluctuations in the column to column average mean column density $(h_m^2\rho_m)$ can be neglected compared to the term $h(\underline{R}')^2\Delta\rho_m$ due to the contrast of the means ($\Delta\rho_m \approx 400\ \mathrm{Kg\,m^{-3}}$). This can be seen by estimating the statistics of the column integrated density fluctuations which for the crust yields $\rho_I \approx h_m\rho_m \approx 13\ \mathrm{Kg\,m^{-3}}$ which is much smaller than $\Delta\rho_m$ (the analogous calculation for the mantle yields a column averaged variation of only 2–3 $\mathrm{Kg\,m^{-3}}$).

Neglecting the $h_m^2\rho_m$ term, we obtain

$$g_z(\underline{R}) \approx -\frac{G\Delta\rho_m}{2}\int_{|\underline{R}-\underline{R}'|>H}\frac{h^2(\underline{R}')d^2\underline{R}'}{|\underline{R}-\underline{R}'|^3}. \tag{D.3}$$

The range of integration must be such as to respect the thin crust approximation ($|(\underline{R}-\underline{R}')| > h(R') > H$; H is the typical thickness; it should be of the order of the largest h values encountered). For these scales the above power law convolution is a fractional differentiation of order 1 (integration order -1), so that in Fourier terms, we have the following relation between 2-D transforms

$$\tilde{g}_z(\underline{K}) \approx -\frac{G\Delta\rho_m}{2}\widetilde{h^2(\underline{K})}K; \quad K < 1/H. \tag{D.4}$$

Taking the complex conjugate equation and multiplying the two and after ensemble averaging, we finally obtain

$$E_g(K) \approx \frac{G^2\Delta\rho_m^2}{4}E_{h^2}(K)K^2; \quad K < 1/H, \tag{D.5}$$

where $E_{h^2}(K)$ is the horizontal spectrum of the square of the thickness. We can estimate the latter by considering that h is a constant thickness h_0 plus a fluctuating part h'

$$h(\underline{R}) = h_0 + h'(\underline{R}), \tag{D.6}$$

so that

$$E_{h^2}(K) = E_{h_0^2}(K) + 4h_0^2E_{h'}(K) + E_{h'^2}(K). \tag{D.7}$$

The term $E_{h_0^2}(K)$ is proportional to $\delta(K)$, and if h_0 is larger than the typical fluctuation, $E_{h'^2}(K) < E_h(K)$, so that

$$E_{h^2}(K) \approx 4h_0^2E_{h'}(K). \tag{D.8}$$

To test the consequences for the gravity spectrum, we can use the topography as surrogate for h'. If we assume that the "roots" of the topography are χ times larger, then we have

$$h'(\underline{R}) = \chi h_t(\underline{R}), \tag{D.9}$$

where h_t is the topography. Overall, we obtain

$$E_g(K) \approx G^2\Delta\rho_m^2h_0^2\chi^2E_{h_t}(K)K^2; \quad K < 1/H, \tag{D.10}$$

i.e., in this range, $E_{h_t}(K) \propto E_{\mathrm{geoid}}(K)$ (see (2.30)), Fig. 6.

References

Blakely RJ (1995) Potential theory in gravity and magnetic applications. Cambridge University Press, Cambridge, pp 441

Bowin C (2000) Mass anomaly structure of the Earth. Rev Geophys 38:355–387. doi:10.1029/1999RG000064

Bullard EC, Cooper RIB (1948) The determination of the mass necessary to produce a given gravitational field. Proc R Soc Lond, Ser A 194:332–347

Busse FH (1989) Fundamentals of thermal convection. In: Peltier WR (ed) Mantle convection, plate tectonics and global dynamics. Gordon and Breach, New York, pp 23–95

Dimri VP, Vedanti N (2005) Scaling evidences of thermal properties in Earth's crust and its implications. In: Dimri VP (ed) Fractal behaviour of the Earth system. Springer, Heidelberg

Fedi M et al (2005) Regularity analysis applied to well log data. In: Dimri VP (ed) Fractal behaviour of the Earth system. Springer, Heidelberg

Gagnon JS, Lovejoy S, Schertzer D (2003) Multifractal surfaces and topography. Europhys Lett 62:801–807. doi:10.1209/epl/i2003-00443-7

Gagnon JS, Lovejoy S, Schertzer D (2006) Multifractal Earth topography. Nonlinear Proc Geophys 13:541–570

Kaula WM (1963) Elastic models of the mantle corresponding to variations in the external gravity field. J Geophys Res 68:4967–4978. doi:10.1029/JZ068i002p00473

Jarvis GT, Pelletier WR (1989) Convection models and geophysical observations. In: Pelletier WR (ed) Mantle convection: plate tectonics and global dynamics. Gordon and Breach, London, pp 479–592

Leary P (1997) Rock as a critical-point system and the inherent implausibility of reliable earthquake prediction. Geophys J Int 131:451–466. doi:10.1111/j.1365-246X.1997.tb06589.x

Leary PC (2003) Fractures and physical heterogeneity in crustal rock. In: Goff JA, Hollinger K (eds) Heterogeneity in the crust and upper mantle. Kluwer Academic, New York, pp 155–186

Lemoine FG, Kenyon SC, Factor JK, Trimmer RG, Pavlis NK, Chinn DS, Cox CM, Klosko SM, Luthcke SB, Torrence MH, Wang YM, Williamson RG, Pavlis EC, Rapp RH, Olson TR (1998) The development of the joint NASA GSFC and NIMA geopotential model EGM96, NASA Goddard Space Flight Center, Greenbelt, Maryland, 20771 USA, July

Lovejoy S, Schertzer D (1998) Stochastic chaos and multifractal geophysics. In Guindani FM, Salvadori G (eds) Chaos, fractals and models, vol 96. Italian University Press, pp 38–52

Lovejoy S, Schertzer D (2007) Scaling and multifractal fields in the solid earth and topography. Nonlinear Process Geophys 14:465–502

Lovejoy S, Pecknold S, Schertzer D (2001) Stratified multifractal magnetization and surface geomagnetic fields, part 1: spectral analysis and modelling. Geophys J Int 145:112–126. doi:10.1111/j.1365-246X.2001.00344.x

Lovejoy S, Schertzer D, Gagnon JS (2005) Multifractal simulations of the Earth's surface and interior: anisotropic singularities and morphology. In: Cheng GB-CQ (ed) GIS and spatial analysis, proc of inter assoc math geology, pp 37–54

Marsan D, Bean CJ (1999) Multiscaling nature of sonic velocities and lithography in the upper crystalline crust: evidence from the KTB main borehole. Geophys Res Lett 26:275–278. doi:10.1029/1998GL900295

Maus S (1999) Variogram analysis of magnetic and gravity data. Geophysics 64:776–784. doi:10.1190/1.1444587

Maus S, Dimri V (1995) Potential field power spectrum inversion for scaling geology. J Geophys Res 100:12605–12616. doi:10.1029/95JB00758

Maus S, Dimri V (1996) Depth estimation from the scaling power spectrum of potential fields. Geophys J Int 124:113–120. doi:10.1111/j.1365-246X.1996.tb06356.x

Naidu P (1968) Spectrum of the potential field due to randomly distributed sources. Geophysics 33:337–345. doi:10.1190/1.1439933

Pecknold S, Lovejoy S, Schertzer D (2001) Stratified multifractal magnetization and surface geomagnetic fields, part 2: multifractal analysis and simulation. Geophys Int J 145:127–144. doi:10.1111/j.1365-246X.2001.00345.x

Pilkington M, Todoeschuck J (1993) Fractal magnetization of continental crust. Geophys Res Lett 20:627–630. doi:10.1029/92GL03009

Pilkington M, Todoeschuck J (1995) Scaling nature of crustal susceptibilities. Geophys Res Lett 22:779–782. doi:10.1029/95GL00486

Poirier JP (1991) Introduction to the physics of the earth's interior. Cambridge University Press, Cambridge, pp 264

Schertzer D, Lovejoy S (1985a) The dimension and intermittency of atmospheric dynamics. In: Launder B (ed) Turbulent shear flow 4. Springer, Berlin, pp 7–33

Schertzer D, Lovejoy S (1985b) Generalised scale invariance in turbulent phenomena. Phys Chem Hydrodyn J 6:623–635

Schertzer D, Lovejoy S (1991) Nonlinear geodynamical variability: multiple singularities, universality and observables. In: Schertzer D, Lovejoy S (eds) Scaling, fractals and non-linear variability in geophysics. Kluwer Academic, Dordrecht, pp 41–82

Shiomi K, Sato H, Ohtake M (1997) Broad-band power-law spectra of well-log data in Japan. Geophys J Int 130:57–64. doi:10.1111/j.1365-246X.1997.tb00987.x

Spector A, Grant FS (1970) Statistical models for interpreting aeromagnetic data. Geophysics 35:293–302. doi:10.1190/1.1440092

Tchiguirinskaia I (2002) Scale invariance and stratification: the unified multifractal model of hydraulic conductivity. Fractals 10(3):329–334. doi:10.1142/S0218348X02001373

Vennig-Meinesz FA (1951) A remarkable feature of the Earth's topography. Proc K Ned Akad Wet Ser B Phys Sci 54:212–228